Organic-Inorganic Hybrid Ammonium Halogenobismuthates and their Piezoelectric Properties

A Thesis
submitted to
Indian Institute of Science Education and Research Pune in partial fulfilment of the requirements for the BS-MS Dual Degree Programme
by

Namonarayan Meena

Indian Institute of Science Education and Research Pune
Dr. Homi Bhabha Road,
Pashan, Pune 411008, INDIA.

December, 2022
Supervisor: Prof. R. Boomi Shankar
Professor
Department of Chemistry

Certificate

This is to certify that this dissertation entitled **"Organic-Inorganic Hybrid Ammonium Halogenobismuthates and their Piezoelectric Properties"** towards the partial fulfilment of the BS-MS dual degree programme at the Indian Institute of Science Education and Research, Pune represents work carried out by **Namonarayan Meena** at Indian Institute of Science Education and Research under the supervision of **Prof. R. Boomi Shankar**, Department of Chemistry, IISER Pune, during the academic year 2021-2022.

Student's signature
Date: 28/10/2022

Supervisor's signature
Date: 28/10/2022

Dedicated to My Sisters

Declaration

I hereby declare that the matter embodied in the report entitled **"Organic-Inorganic Hybrid Ammonium Halogenobismuthates and their Piezoelectric Properties"** are the results of the work carried out by me at the Department of Chemistry, Indian Institute of Science Education and Research, Pune, under the supervision of **Prof. R. Boomi Shankar** and the same has not been submitted elsewhere for any other degree.

Student's signature
Date: 28/10/2022

Acknowledgements

I am enormously grateful to my thesis advisor and supervisor, Prof. R. Boomi Shankar, who has been instrumental in guiding my master's project and providing all the necessary resources to complete this thesis. I have had a great learning experience working with him for my MS program.

I am also thankful to my TAC member, Prof. Nirmalya Ballav, for his invaluable input in determining my research goals and keeping me encouraged, motivated, and focused on my project's objectives. I sincerely thank Dr. Jan K. Zaręba (Wroclaw, Poland) for his cooperation and help to perform the SHG experiments.

I express my deepest gratitude to all my lab mates for all the help. I specially thank Mr. Rishabh Gupta, Ms. Cavya Jose, Mr. Rishu Kumar Pandey, Mr. Nilotpal Deka, Mr. Vikash Kushwaha, Mr. Abhradeep Sarkar, Dr. Ranita Samanta, Ms. Meghamala Sarkar, and Ms. Neetu Prajesh for their support, and most importantly the environment provided by them.

I want to thank Supriya Sahoo, I will always be grateful for your kindness. It would be impossible to count all the ways you've helped me in this project and my life. Thank you so much for all that you've done. Thanks for being a good mentor, sister and for guiding me throughout this MS project. I want to thank all of my friends for always being with me in every situation.

Ultimately, I want to thank my family for their precious love and support.

Table of Contents

LIST OF FIGURE

LIST OF SCHEMATIC

LIST OF TABLE

Abbreviation

MEMS	Micro-electro-mechanical Systems
KDP	Potassium Dihydrogen Phosphate
PZT	Lead Zirconate Titanate
Fe-RAM	Ferroelectric Random-access Memories
Fe-FET	Ferroelectric Field-effect Transistors
PLA	Polylactic Acid
SCXRD	Single-crystal X-ray Diffraction
PXRD	Powder X-ray Diffraction
TGA	Thermo-gravimetric Analysis
DTA	Differential Thermal Analysis
DSC	Differential Scanning Calorimeter
FE-SEM	Field-emission Scanning Electron Microscopy
SHG	Second Harmonic Generation
HS	Hirshfeld Surface
PVDF	Polyvinylidene difluoride
I_{PP}	Peak-to-peak Short-circuit Current
V_{PP}	Peak-to-peak Voltages

ABSTRACT

Organic-inorganic hybrid perovskite materials have been widely used due to their unique properties, such as their biocompatibility, photovoltaic, piezo-, pyro- and ferroelectric properties. Their numerous utilizations include solar cells, charge storage capacitors, MEMS, field-effect transistors, resonators, sensors, etc., making them an exciting topic of research. Traditional lead oxide-based ferroelectrics are the most used materials for these applications, but they lead to certain environmental concerns regarding the recycling and disposal of devices. Additionally, literature has many polymers like polyvinylidene difluoride (PVDF) based nanogenerator devices with excellent output performances. But PVDF-based nanogenerators require external additives like poling, annealing etc., to enhance their mechanical outputs. Hence it is highly desirable to prepare all-organic or hybrid organic-inorganic materials with mouldable optical properties and with no toxic metal ion contents for future generation electronics. Here in, we have synthesized two halogenobismuthates(III) molecular–ionic complexes with the general formula A_2MX_5 and $A_3M_2X_9$, which are ferroelectric active and can find their extensive applications in piezoelectric nanogenerator devices. The compound $[BrPhBnN(Me)_2]_2$. $[BiBr_5]$ (**1**) and $[BrPhMeBnN(Me)_2]_3.[Bi_2Br_9]$ (**2**) were crystallised in orthorhombic *Pna2₁* and *Pca2₁* space groups respectively.

The composite nanogenerator devices of **1** and **2** in polylactic acid (PLA) gave maximum peak-to-peak voltages (V_{PP}) of 26.2 V and 24.2 V respectively. Also the maximum power density values were calculated to be 41.81 and 61.88 $\mu W.cm^{-2}$ for the optimal 15 wt% **1-PLA** and 10 wt% **2-PLA** devices, respectively. For compound **1**, 14 and 114 µC charges and 10 and 64 µJ of energy have been stored, respectively, for 10 and 100 µF capacitors. While for compound **2**, 2.03 and 18.92 µC charges and 0.20 and 1.78 µJ of energy has been stored in 10 and 100 µF capacitors, respectively.

1 Introduction:

1.1 Dielectric Materials:

Dielectric materials are electrical insulators that possess no flow of current. Molecules always have some energy, and this causes random motion. At equilibrium, there is random motion in any one direction that is equal in the opposite direction, so the average positions of the molecules remain constant. As there is an electric field on dielectric material due to electrostatic forces, the atom's positively charged nucleus and negatively charged electrons shift from their equilibrium position and generate a non-zero dipole moment [Figure 1]. The total dipole moment over a unit volume is called polarization.

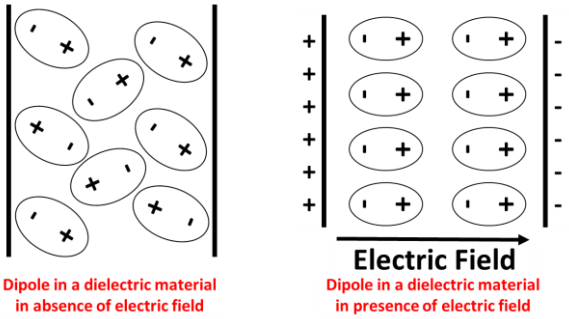

Figure 1: Effect of external electric field on dielectric materials.

1.2 Polarizations Mechanisms:

Electronic (or Optical) Polarization:

While applying an external electric field to a molecule, its nucleus and electron displace from their equilibrium position, which leads to generate a tiny dipole that leads to a slight change in polarization.

Ionic (or Atomic) Polarization:

If an electric field is applied to an ionic molecule, then the ionic bond gets stretched, which leads to a change in dipole and polarization of the molecule.

Orientational (or Dipolar) Polarization:

If an electric field is applied to a dipolar molecule, then dipoles get align themselves in the particular direction of the electric field, leading to the polarization of the molecule.

Space Charge (or Interfacial) Polarization:

While applying an external electric field to a material, then mobile charged particles (positively and negatively) migration happens and produces an interface of charge, cause an extrinsic type of polarization.

1.2.1 Dependency of Frequency on Polarization:

Each type of these polarizations has different time response capability for the frequency of an applied external electric field.[1, 2] Electronic displacements can happen rapidly so that polarization can occur even at frequencies up to 10^{17} Hz. At the same time, ionic polarization is a bit slower and occurs up to 10^{13} Hz frequencies. While dipole polarization occurs at relative lesser than 10^{10} Hz frequencies. Space charge polarization is the slowest and occurs at less than 10^{4} Hz frequencies [Figure 2].

While increasing the frequency, the polarization mechanisms become comparatively less effective, so dielectric constant (the ability of the material to polarise) decreases, giving rise to lower dielectric constants.

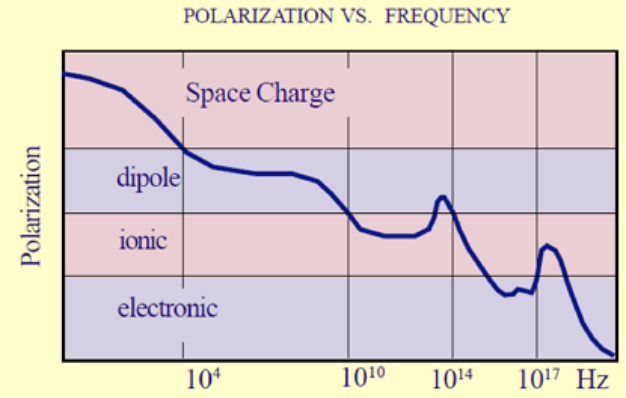

Figure 2: Effect of frequency on different types of Polarization (Ref. 25).

1.2.2 Dependency of Temperature on Polarization:

Upon increasing temperature, the molecules have more kinetic and thermal energy, which results in an increased thermal motion for dipoles and the deviation from a field's perfect alignment becomes more significant. As a result, the molecules becomes less closely aligned with one another, and hence the materials' orientational polarization and dielectric constant decrease. While in ionic systems, increasing temperature leads to increases in ion mobility, enhancing the polarization and dielectric constant. This is not always true that polarization and dielectric constant decrease while increasing temperature. In dipolar systems, higher temperatures are associated with more thermal agitation, which works against the dipolar polarisation mechanism, which is why the polarisation tends to decline as temperature rises. Electronic polarization is relatively insensitive to temperature. There are many discontinuities in the dielectric constant as temperature changes. The dielectric constant depends on the structure, so the dielectric constant suddenly changes at the phase boundary.

1.3 Types of Dielectrics:

There are 14 Bravais lattices, using different-different combinations of these Bravais lattices with symmetry operations (inversion, rotation and screw axes, glide planes, and mirror planes); there are only 230 unique combinations for three-dimensional symmetry. All 230 three-dimensional space groups are distinctive.

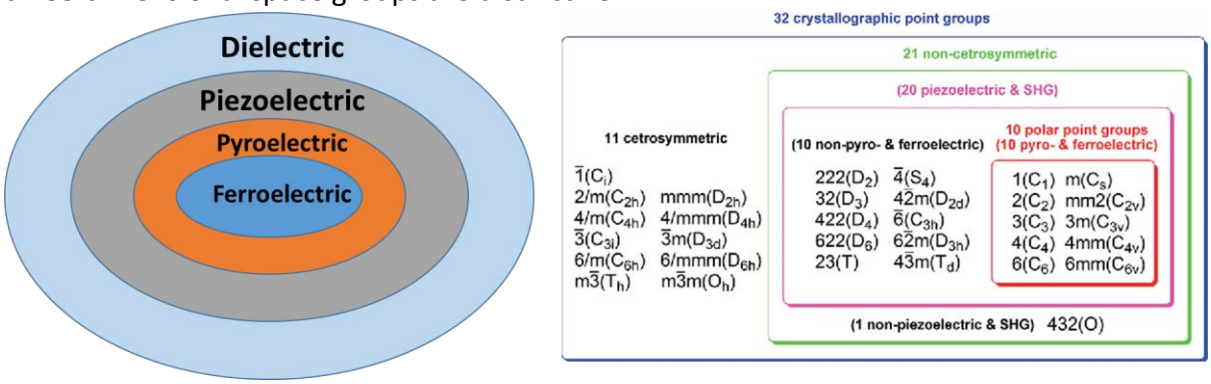

Figure 3: Types of dielectric materials (Ref. 24).

A total of 32-point groups are there; out of them, 11 have an inversion center, giving rise to centrosymmetric crystal structures. The remaining are noncentrosymmetric in nature, possessing no inversion center. 20 among these noncentrosymmetric point groups exhibit piezoelectricity, and only ten of them show pyro- and ferroelectricity [Figure 3].[3]

Linear Dielectrics: The extent of polarization (dielectric constant) increases linearly while increasing the applied electric field, leading to a rise in polarization.

Nonlinear dielectrics: The dielectric constant doesn't respond to an applied external electric field linearly and has large dielectric constants. Even in the absence of the electric field, these dielectrics have a non-zero polarization.

A. Piezoelectric Materials:

Nonlinear dielectric materials in which electric charges are accumulated on the material's surface as a response to the applied mechanical stress are called piezoelectric materials. The piezoelectric effect uses the material to convert mechanical energy into electric energy, or visa-versa. Similarly, if the electric potential is provided to the surface of a piezoelectric material, there will be charge accumulation. As a result, there will be some mechanical deformations in the material.

B. Pyroelectric Materials:

Nonlinear dielectric materials in which electric charges are accumulated on the material's surface in response to applied uniform thermal stress are called pyroelectric materials. The pyroelectric effect uses the material to convert thermal energy into electric energy, or visa-versa. As the thermal and kinetic energy of the material increases, the amplitude of the random thermal motion of dipoles increases, resulting in charge accumulation on the surface. Similarly, suppose the electric potential is provided to the surface of pyroelectric material. In that case, there will be charge accumulation on the surface and some thermal change in the material.

C. Ferroelectric Materials:

Ferroelectric materials are a class of non-linear dielectrics that possess a spontaneous polarization and polarization reversal in the presence of an external applied electric field.[4] These nonlinear dielectric materials are a subclass of piezo- and pyroelectric materials depending on the symmetry of material in space.

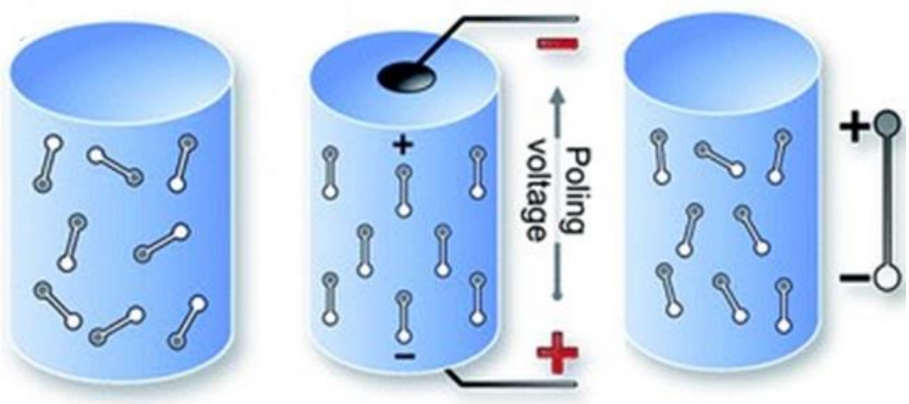

Figure 4: Poling mechanism (Ref. 24).

Initially, all the dipoles of ferroelectric material are randomly oriented; upon applying an external electric field, the dipoles start to align in a particular direction and reach a saturation state [Figure 4].

The application of an electric field generates a rectangular P-E hysteresis loop in ferroelectric materials. The randomly oriented dipoles lead to no net polarization at point *O* in the ferroelectric system. Upon applying an electric field externally, the domains start to orient along with the direction of the applied electric field and reach a saturation state where all domains get aligned in a particular direction($O \rightarrow P_s$). This state where all domains are aligned in single direction is called saturation polarization (P_s). The polarization does not demolish to zero on removal of electric field due to the kinetic arrest of polar domains ($P_s \rightarrow P_r$). The amount of polarization that remains in the material after the removal of external electric field is called Remnant polarization (P_r).

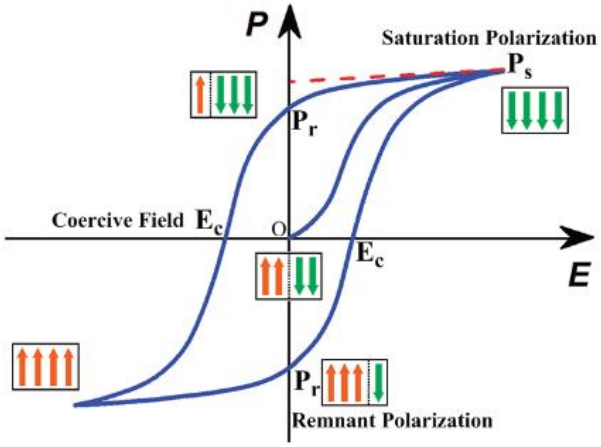

Figure 5: Potential-Electric field hysteresis loop (Ref. 24).

Further, if an opposite-directional external electric field , called as coercive electric field (E_c) is applied to the molecule, the system reverts to the initial state of zero polarization.[3] Further, if the application of electric field in the opposite directional, completes the hysteresis loop [Figure 5].

1.4 History of Ferroelectrics:

Joseph Valasek was the first person to explore the ferroelectric hysteresis nature of Rochelle salt (potassium sodium tartrate tetrahydrate, $KNaC_4H_4O_6.4H_2O$) in 1920.[4] Due to its resemblance with ferromagnetism, this term called as "ferroelectric". It was the only known ferroelectric material for a very long period until Scherrer and Busch explored the ferroelectric behaviour in potassium dihydrogen phosphate (KDP, KH_2PO_4) in 1935.[5] However, the low ferroelectric polarization, instability, and poor crystal stability under ambient conditions prevented the technological application of these materials.

Barium titanate ($BaTiO_3$) is first known non-hydrogen bonded perovskite ferroelectric ceramic material, it was discovered in 1940.[6] After the discovery of $BaTiO_3$, a lot of ferroelectric ceramics such as $Pb(Zr, Ti)O_3$ (PZT), $LiTaO_3$(LTO), $LiNbO_3$ (LNO), $KNbO_3$ (KNO), etc. were discovered, Then these materials with remarkable ferroelectric polarization occupied the mainstream.[7, 8]

1.5 Applications of Ferroelectric Materials:

Due to many-sided physical properties such as piezoelectricity, pyro-electricity, dielectric and nonlinear optical behaviour, ferroelectric materials unroll various applications.[9-12]

Owing to the inherent piezoelectric nature, ferroelectric materials are frequently used in transducers, actuators, micro-sensors, micro speakers, MEMS, microphones, etc.

The most extensive property of these materials that forms as foundation for their use in ferroelectric field-effect transistors (Fe-FET) and ferroelectric random-access memories (Fe-RAM) is their polarization switchability under an applied external electric field.[13, 14]

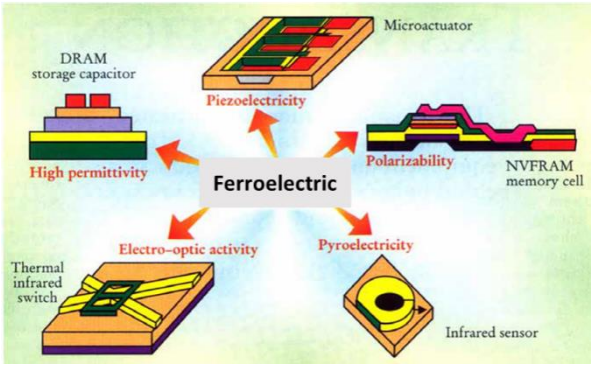

Figure 6: Applications of ferroelectric materials (Ref. 26).

They also describe the basis for several scientific tools, including time reference sources in quartz watches, and atomic force microscopy etc. These materials form appealing candidates for infrared detectors and thermal imaging due to their pyroelectric intrinsic characteristics. Their high dielectric permittivity opens the way for constructing dielectric resonators and capacitors.

1.6 Organic-Inorganic Hybrid Ammonium Halogenobismuthates and their Piezoelectric Properties:

Hybrid organic-inorganic crystalline materials are of great interest because they frequently exhibit ferroelectric properties.[10, 12] Energy harvesting from mechanical vibrations via the piezoelectric effect or from temperature fluctuations via the pyroelectric effect is particularly interesting for ferroelectric materials. The interest in energy harvesting from ambient sources has grown recently for micro-electromechanical devices (MEMS) and wireless electronics. Self-powered systems are particularly interested in reducing the use of batteries, the current power source of choice for sensors. Still, their finite lifespan can quickly add to the maintenance cost of these systems. Due to their limited lifetime, frequent replacement of batteries is a time-consuming, complex, and expensive process.

The ability to extract energy from the surrounding environment using piezoelectric or pyroelectric devices offers a potential mode for powering small-scale electronic devices without the wire to supply power. [16] Alternatively, mechanical and thermal energy harvesting could be used to recharge batteries, reducing problems associated with their disposal and significantly extending their lifetime.

Due to their excellent piezoelectric properties, ferroelectrics based on lead oxide are the most used nonlinear materials as transducers, sensors and actuators.[6, 7, 15] However, there are associated concerns about the disposal and recycling of devices containing PZT because its oxide (lead oxide, PbO) forms and vaporizes during the processing in presence of oxygen. These oxides stay in the environment for a long time and accumulate in the organisms, causing damage to the lungs, liver, spleen, brain and nervous system.[16] PZT itself does not seem toxic to cells, but if it dissolves in the presence of cytoplasm releases lead ions and makes clusters inside the cytoplasmic vesicles while in the liver, kidney, and brain shows

tissue specific subcellular processing. Previous studies reveal that ceramics containing PZT dissolved in water have shown the presence of lead ions (Pb^{2+}) in the water. Hence, psychological solid reluctance to introduce lead-containing products into the human body should also be considered. [16]

Thus, there is an increasing approach to look for alternative materials with no toxic metal contents. Sensors are implanted directly into living tissue, so there is a need for developing environment-friendly and biocompatible piezoelectric materials. Researchers around the globe have synthesized a lot of ammonium and phosphonium-based organic and hybrid organic-inorganic materials, which can overcome the disadvantages of ancient ceramics. Hybrid ferroelectric materials exhibit advantages like tuneable band gap, long diffusion length, high carrier mobility, strong optical absorption, and high solution processability and thus can be utilized in photovoltaics as solar cells.[14] In our lab, we successfully synthesized all organic materials like DPDP.PF_6, TPAP.BF_4, and DPDP.BF_4. These materials gave rise to excellent piezoelectric energy harvesting outputs of the order of 7.37, 8.95, and 4.75 V.[17-20] Also, organic-inorganic hybrids like $[Me_3NCH_2CH_2OH].CdCl_3$ and $[^sCH(MePh)(Me)NH_3].[BiBr_5]$ have been reported with significant output performances.[21, 22] Keeping all these in mind, we explore other organic-inorganic bismuth-based ammonium salts and their applications in energy harvesting. Herein, we have synthesized two halogenobismuthates(III) molecular–ionic complexes with the general formula$A_2MX_5$and $A_3M_2X_9$ (where A, M, and X denote organic cation, metal, and halogen atoms, respectively). The synthesized compounds $[BrPhBnN(Me)_2]_2$. $[BiBr_5]$ (**1**) and $[BrPhMeBnN(Me)_2]_3.[Bi_2Br_9]$ (**2**) crystallize in *Pna21* and *Pca21* space groups and are suitable for piezo- and ferroelectric analyses. The anionic substructure in both compounds plays a vital role in the generation of noncentrosymmetric properties. Their anion moieties have a wide range of stoichiometry, connectivity and geometries. A characteristic feature of **1** is the presence of various bi-octahedral anionic units (MX_5) containing only one bridging halogen atom in the structure to form endless trans-connected one-dimensional chains. Also, in compound **2**, the bismuth ion is in a hexa-coordinated bi-octahedral geometry giving rise to an $A_3M_2X_9$ system. Further, the bulk purity of these materials is investigated through powder X-ray diffraction (PXRD) analyses. These materials were found stable up to around 154 ˚C and 134 ˚C, respectively for **1** and **2** as depicted from their thermos gravimetric (TGA) and differential thermal analyses (DTA) profiles. The compounds were examined for their dielectric activity in different frequency and temperature combinations. Dielectric permittivity of 9.51 and 7.49 for compounds **1** and **2** were recorded at room temperature(RT) and 10^5 Hz frequency. Additionally, the polymer composites were prepared from compounds **1** and **2** (5, 10, 15, and 20 wt%) with the polymer polylactic acid (PLA). These composite films were tested for energy-harvesting applications. The maximum output voltages were obtained to be 26.2 and 24.06 V for 15 wt% **1-PLA** and 10 wt% **2-PLA,** respectively. Further, their practical utility has been investigated by charging 10 µF and 100 µF capacitors. For 15 wt% **1-PLA**, 14 µC and 114 µC charges and 10 µJ and 64 µJ of energy have been stored, respectively, for 10 µF and 100 µF. In comparison, 10 wt% **2-PLA** has stored 2.03 µC and 18.92 µC charges and 0.20 µJ and 1.78 µJ of energy for 10 µF and 100 µF, respectively.

2 Material and Methods

2.1 General Remarks:

The purchased 4-Bromo-N,N-dimethylaniline and 4-methylbenzylbromide from Sigma chemicals were used without further purification. The purchased Benzyl bromide from Lobachemie was also used with no additive purification. Other starting materials like bismuth (II) oxide and hydrobromic acid were purchased from Avra Chemicals.

2.2 Characterisation:

2.2.1 Crystallography:

The SCXRD data were obtained from Bruker Smart Apex Duo diffractometer using Mo Kα radiation (λ = 0.71073 Å). Using Apex 3 program, crystal structures were solved, and the refinements were done using SHELXL-2014/7 built in the Apex 3 program by full-matrix least-squares against F2.[23] All the non-hydrogen atoms were refined anisotropically. Hydrogen atoms were constructed in geometric positions to their parent atoms. Using DIAMOND-3.1 software, structural images were prepared. Using Bruker-D8 Advance X-ray diffractometer, the powder X-ray diffraction (PXRD) data were measured from 5 to 50° in the 2θ range.

2.2.2 Thermal Analysis:

Melting point analyses for **1** and **2** were done using a Buchi M-560 melting point apparatus and were uncorrected. Thermal analysis data was acquired using a PerkinElmer STA6000 thermo-gravimetric analyzer and TA Q20 differential scanning calorimeter (DSC) at a heating rate and cooling rate of 10 °C/min in a nitrogen atmosphere.

2.2.3 FE-SEM Analysis:

Using the Zeiss ultra plus FE-SEM instrument, the Field-emission scanning electron microscopy (FE-SEM) analysis of all ferroelectric composite films (all different wt%) of compounds **1** and **2** was performed with a minimum spatial resolution of 2 µm.

2.2.4 Dielectric and Piezoelectric measurements:

Powder sample of compounds **1** and **2** were compacted into pallets of 1.53 mm (**1**) and 1.48 mm (**2**) thicknesses with 8 mm diameter, respectively to determine the dielectric properties. Later, copper adhesive tapes were attached to the pallets, which eventually acted as electrodes for both measurements. Using the Solartron Analytical Impedance Analyzer 1260 coupled with a Dielectric Interface 1296A operating with Janis 129610A cryostat sample holder and a Lakeshore 336 model temperature controller, these experiments were performed. The frequency-dependent dielectric measurements were carried out in cooling run at different temperatures.

2.2.5 Nonlinear optical measurements:

Using an attenuated output from a Coherent AstrellaTi:Sapphire regenerative amplifier providing 1300 nm laser pulses at 1 kHz repetition rate and 75 fs duration, SHG measurements were performed. For these optical measurements, the Kurtz-Perry setup was used at room temperature, where Potassium dihydrogen phosphate (KDP) was used for the reference for second harmonic generation (SHG).

2.2.6 Piezoelectric Energy Harvesting Measurements:

Piezoelectric tests were performed using a custom-built impact instrument. While output voltages were measured using a Tektronix 4034 Digital Phosphor Oscilloscope operating at an input impedance of 1 MΩ. The devices' active area under test and thickness were 3 cm^2 and ~1.5 mm, respectively.

2.2.7 Dipole Moment Calculations:

Using Gauss view, multilayer ONIOM model calculation for dipole moment and total energy of molecule was calculated. For these calculations, the cationic parts were selected as the lower layer, and the anionic parts as the high layer. SDD basis set was used for quadratically convergent {Keywords used for calculation: ONIOM(B3LYP/SDD:PM6) scf=qc geom=connectivity}.

2.3 Synthesis of Crystal 1:

2.3.1 Synthesis of Ligand [BrPhBnN(Me)$_2$].Br (L1):

Benzylbromide (0.5 ml, 4 mmol) in hexane was added to a stirred solution of 4-Bromo-N,N-dimethylaniline (800 mg, 4 mmol) in 5 ml of hexane. The resulting solution was stirred for 30 minutes, and the white precipitate of [BrPhBnN(Me)$_2$].Br (**L1**) was collected after solvent evaporation. White crystals of ligand were obtained from a solution of acetone and acetonitrile.

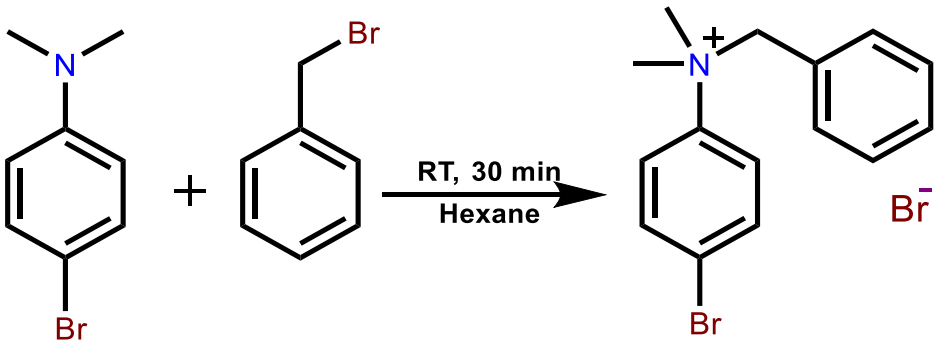

Scheme 1: Schematic for L1 preparation.

2.3.2 Synthesis of [BrPhBnN(Me)$_2$]$_2$. [BiBr$_5$]:

The bromide salt [BrPhBnN(Me)$_2$].Br(900 mg, 3 mmol) was dissolved in concentrated HBr and subsequently added in a dropwise manner to a solution of Bi_2O_3 (705 mg, 1.5 mmol) in concentrated HBr [Scheme 2]. The resulting solution was stirred for 30 minutes, and the yellow precipitates of [BrPhBnN(Me)$_2$]$_2$. [BiBr$_5$] (**1**) was collected.

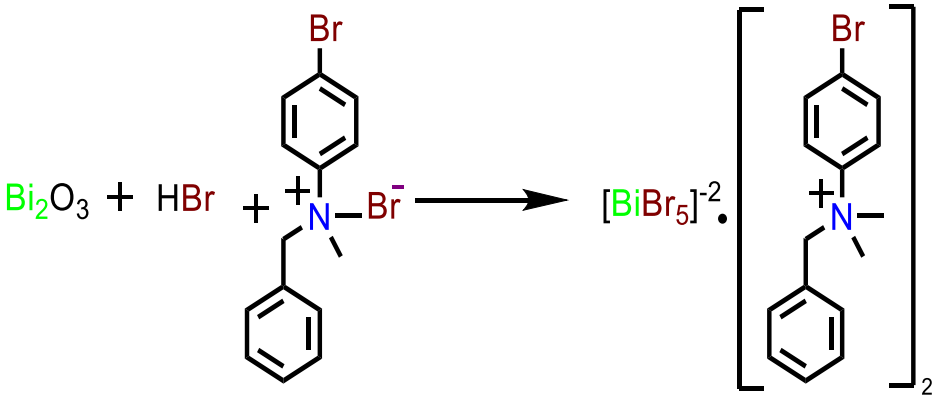

Scheme 2: Schematic for the preparation of **1.**

Suitable yellow crystals of **1** for single crystal X-ray analysis were obtained from acetonitrile and acetone (1:1) containing solution after two days.

2.4 Synthesis of Crystal 2:

2.4.1 Synthesis of Ligand [BrPhMeBnN(Me)$_2$].Br (L2):

A similar procedure was followed for the preparation of **L2**. Here, 4-methylbenzylbromide (555 mg, 3 mmol) in 1 ml hexane was added to a stirred solution of 4-Bromo-N,N-dimethylaniline (600 mg, 3mmol) in 4ml of hexane. The solution was stirred for 30 minutes, and the white precipitate of [BrPhMeBnN(Me)$_2$].Br (**L2**) was collected. White crystals of L2 were obtained from a solution of acetone and acetonitrile.

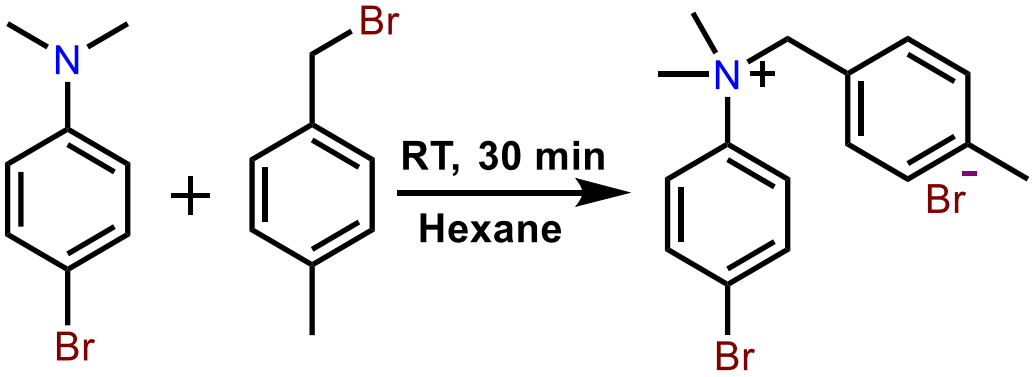

Scheme 3: Schematic of L2 preparation.

2.4.2 Synthesis of [BrPhMeBnN(Me)$_2$]$_3$.[Bi$_2$Br$_9$]:

The bromide salt (795 mg, 2.6 mmol) was then dissolved in excess HBr and was added dropwise to a solution of Bi_2O_3 (2.363 gm, 1 mmol) in concentrated HBr. The resulting solution was again stirred for 30 minutes, and the yellow precipitate of [BrPhMeBnN(Me)$_2$]$_3$.[Bi$_2$Br$_9$] (**2**) was collected [Scheme 4]. Suitable yellow crystals of **2** for single crystal X-ray analysis were obtained from acetonitrile and acetone (1:1) containing solution after two days.

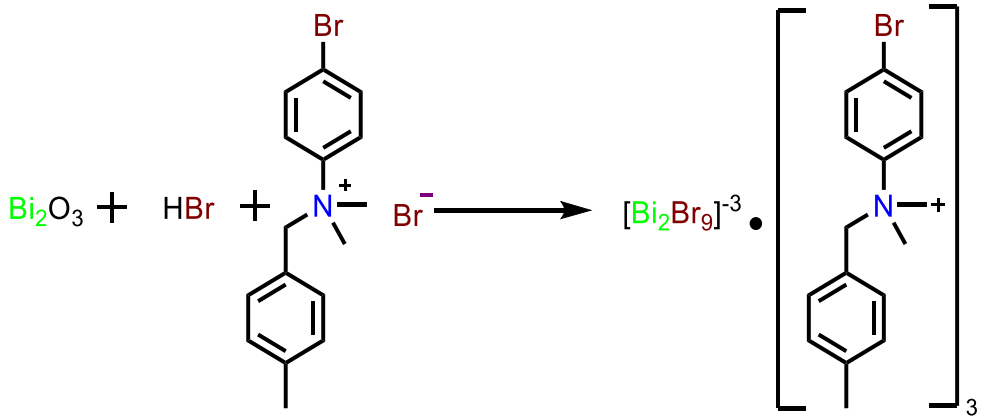

Scheme 4: Schematic for the preparation of **2.**

2.5 Synthetic procedure for the polymer composite film preparation:

Encouraged by the earlier reported nanogenerator applications on similar kinds of hybrid perovskites, the ammonium slats **1** and **2** were investigated for their corresponding applications in piezoelectric energy harvesting. Polylactic acid (PLA) was used to make the polymer composites of **1** and **2**.

PLA was dissolved in chloroform, and different percentages (5, 10, 15, and 20 wt%) of **1** and **2** were dispersed in chloroform ($CHCl_3$). The mixture was left to stir for 35 minutes, followed by 15 minutes of vortex mixing to attain homogeneity of the polymer composite solution. Then solutions were poured onto the petri dish and were kept at room temperature until they dried. Subsequently, the films were peeled off from the glass surface of the petri-dish.

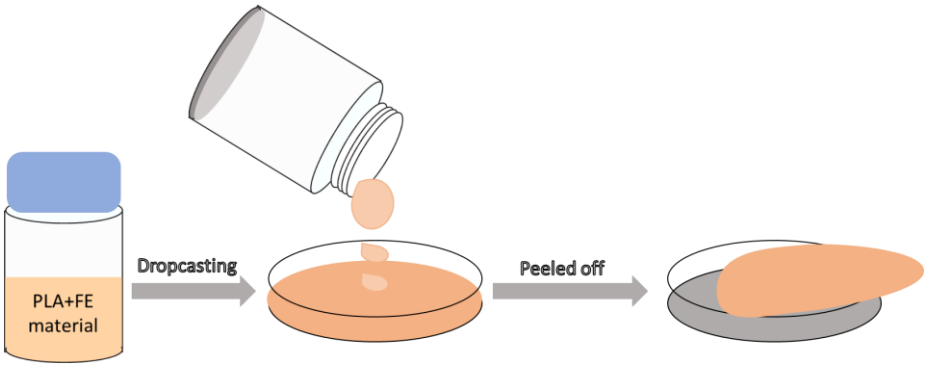

Scheme 5: Schematic diagram for the preparation of **PLA** composite films.

These films were embedded on both sides for nanogenerator device applications using adhesive copper tapes, and copper wires were used as electrodes. After that these devices were embedded with Kapton tapes completely to avoid direct contact from the constant hammering process during the measurement. A similar device of neat PLA was also made for comparison.

3 Result & Discussion

3.1 X-ray crystallographic data of 1 and 2:

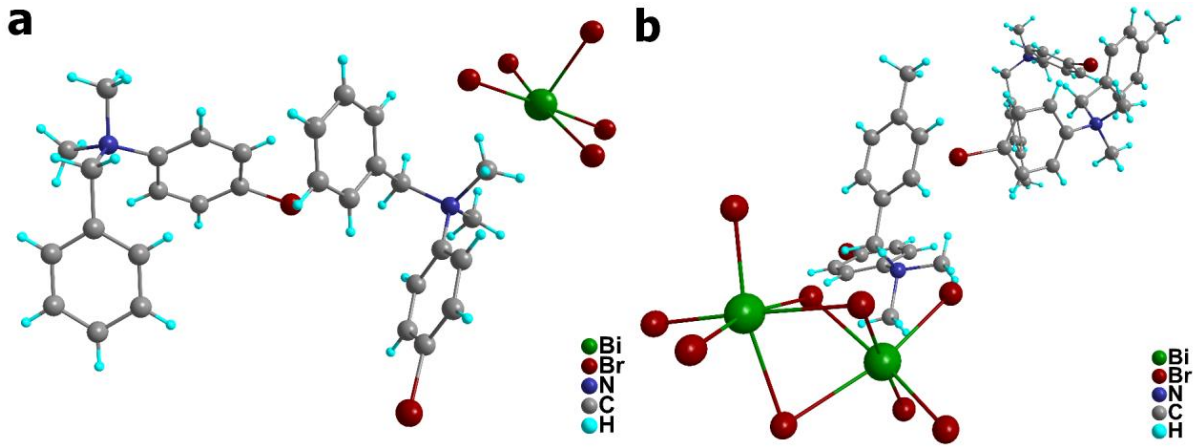

Figure 7: Molecular structures of a) **1** and b) **2** at 100 K

The compounds **1** and **2** synthesized from ligands **L1** and **L2** were crystallized in noncentrosymmetric polar orthorhombic *Pna2₁* and *Pca2₁* space group, respectively, at 100 K. The asymmetric unit of compound **1** consists of two ammonium cations units supported by one $[BiBr_5]^{2-}$ [Figure 7a]. While the asymmetric unit of compound **2** consists of a $[Bi_2Br_9]^{3-}$ anionic subunit supported by three ammonium cations [Figure 7b].The noncentrosymmetry in these two ammonium analogues are attributed to the anionic substructure in both the compounds.

The anionic moiety of **1** corresponds to a discrete bi-octahedral anionic unit ($BiBr_5$) comprising with only one bridging Br-atom in the structure to form endless trans-connected one-dimensional chains. Also, in compound **2**, the bismuth ion is in a hexa-coordinated bi-octahedral geometry giving rise to an $A_3M_2X_9$ perovskite system. These attributes from the anionic moieties contribute to the noncentrosymmetry in **1** and **2,** making them suitable for ferro- and piezoelectric analyses.

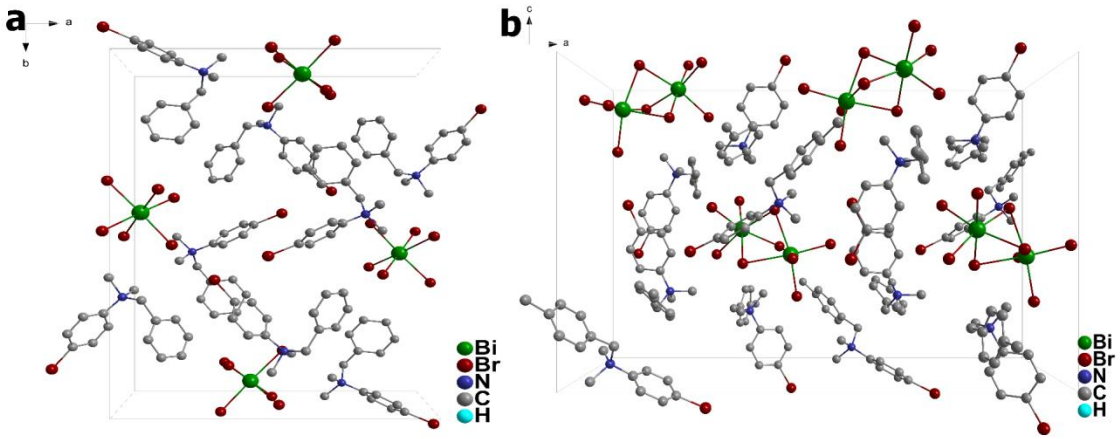

Figure 8: Packing diagrams of a) **1** along the c-axis b) **2** along the b-axis at 100 K.

Further, the bulk purity of compounds **1** and **2** were confirmed from PXRD analyses, where a good match of the simulated ones with the as-synthesized ones was observed [Figure 9].

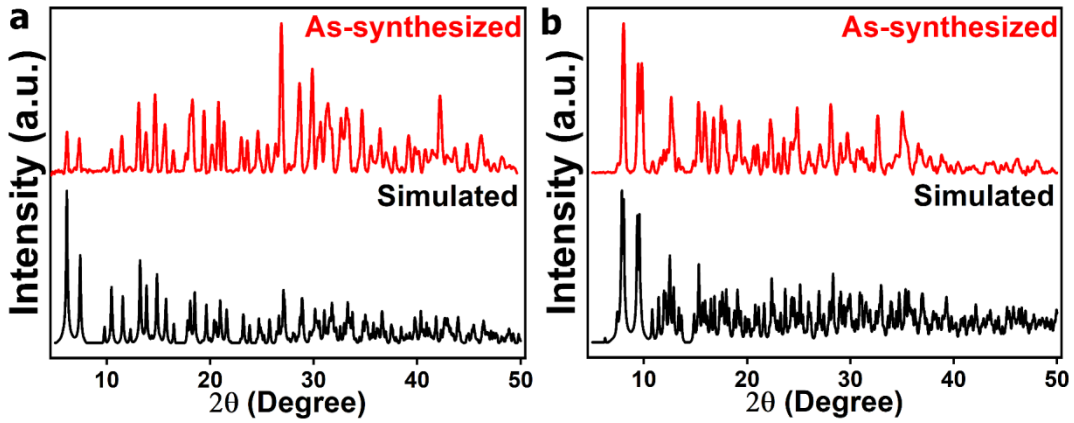

Figure 9: Stacked PXRD profile (experimental and simulated) of a) **1** and b) **2** at room temperature.

Stacked PXRD profiles of **1**–TPU films and their comparison with the diffraction patterns of **1** However, the ionic interactions and hydrogen bonding (C-H···Br) are responsible for robust long-range order with structural stabilization of **1** and **2**.

A closer look at the H-bonding interaction figure reveals that methyl and methylene proton of ammonium cations interact with the Br atom of $[BiBr_5]^{2-}$ in **1**. While in **2**, the para C-H groups and methyl protons of the ammonium cation interact with the terminal bromine atoms of the $[Bi_2Br_9]^{3-}$ unit, leading to non-classical H-bonding interactions [Figure 10].

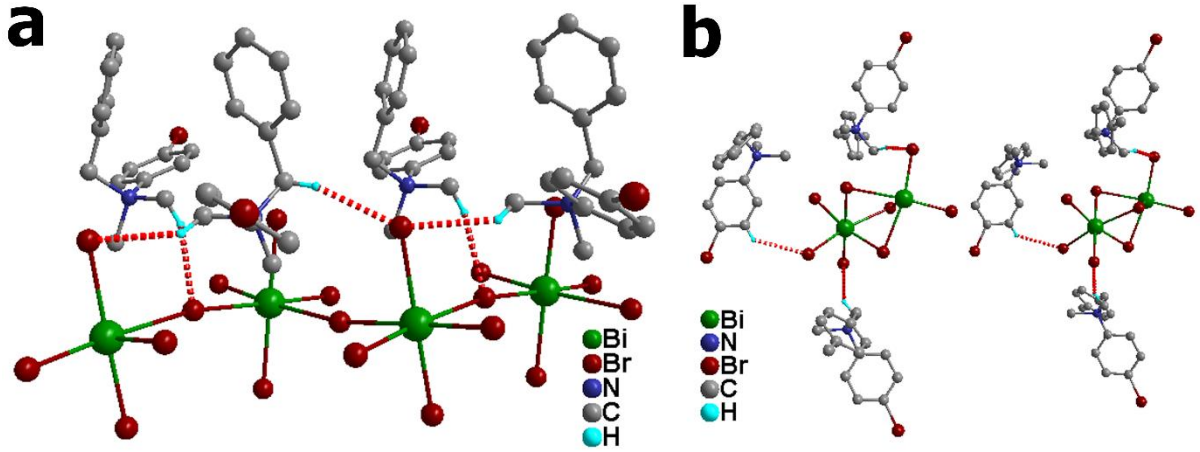

Figure 10: The hydrogen bonding interactions in a) **1** and b) **2** mediated by C–H···Br interactions.

3.2 Thermal Analysis:

TGA and DTA profiles: The thermogravimetric analysis (TGA) and differential thermal analysis (DTA) revealed that compound **1** is stable up to around 154 ˚C while **2** is stable up to 134 ˚C [Figure 11].

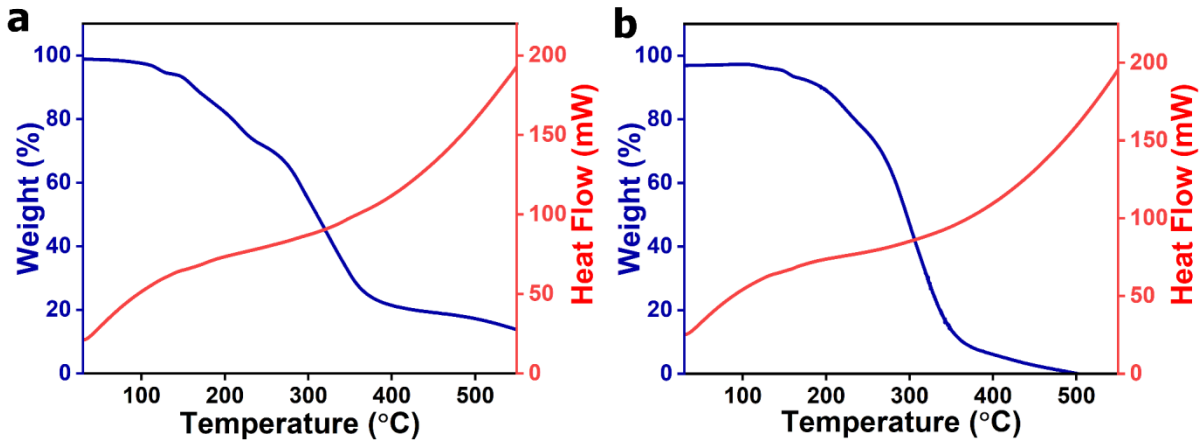

Figure 11: Thermal profiles TGA (blue), DTA (red) of a) **1** and b) **2.**

The manual melting point measurements depicted that the melting temperatures for compounds **1** and **2** fall in the range of 154-158 ˚C and 134-138 ˚C, respectively. To investigate the structural changes (Morphotropic Phase Boundary/phase transition) as a result of temperature changes, the differential scanning calorimetry (DSC) measurements were performed. The DSC analyses on the powder samples of **1** and **2** confirmed no heat anomalies in both the compounds up to their corresponding melting temperatures.

3.3 SHG Measurements:

The unsieved powder samples of **1** and **2** gave second harmonic generation (SHG) efficiencies of 0.039 and 0.11, respectively, with respect to the reference KDP [Figure 12]. These measurements confirmed the noncentrosymmetric nature of **1** and **2** at room temperature.

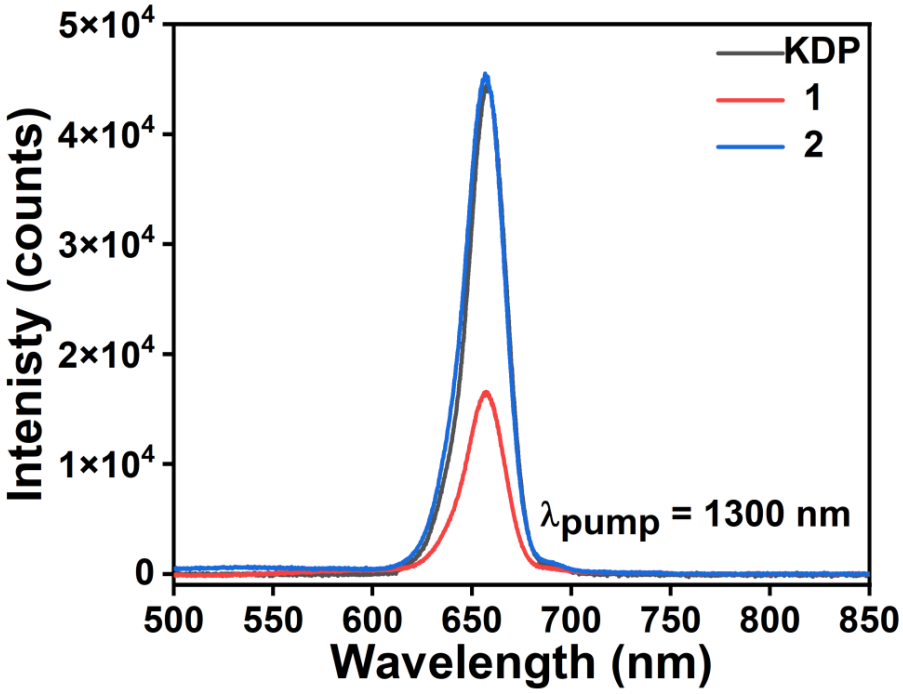

Figure 12: SHG plot of **1** and **2** with respect to KDP at 1300 nm pump.

3.4 Theoretical calculation for 1 and 2:

From the ONIOM calculations, the total energy and dipole moment for **1** were obtained to be -71.82 Hartree and 37.10 Debye, respectively. Similarly, for compound **2**, the total energy and dipole moment were calculated to be -130.35 Hartree and 115.07 Debye, respectively. These theoretical calculations certify the polar nature of compounds **1** and **2** for their further studies on ferroelectric and piezoelectric characterizations.

3.5 Dielectric Studies:

Furthermore, the dielectric nature of **1** and **2** were investigated below the melting temperature (378 K) and in 10-10^5 Hz frequency range. For compounds **1** and **2**, the dielectric constants were found to be 9.51 and 7.49 at room temperature and 100 kHz frequency [Figure 13].

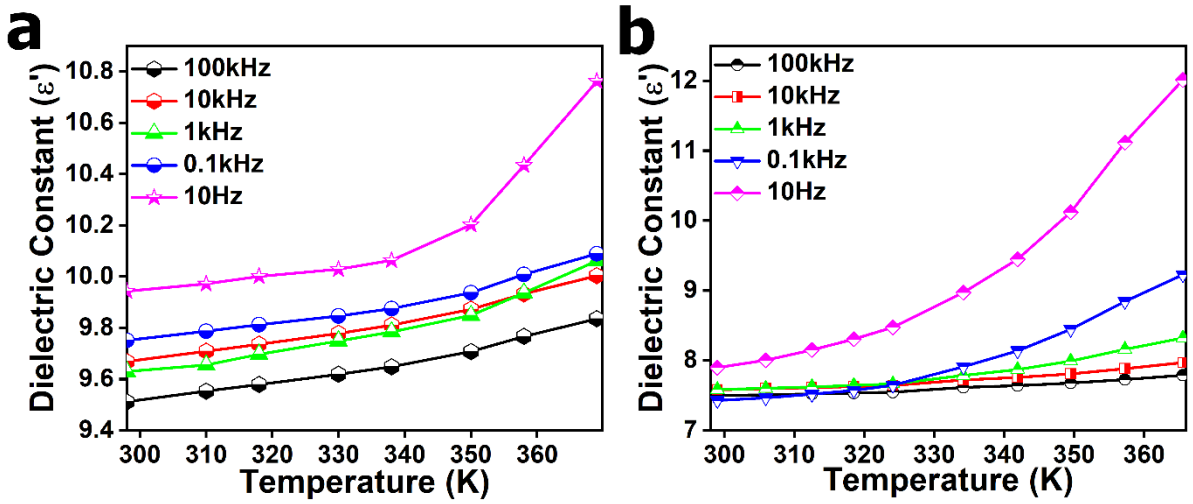

Figure 13: Temperature dependence of dielectric constant a)**1** and b) **2**.

The value of ε' for **1** and **2** showed increasing trends while increasing the temperature close to their melting temperatures owing to the enhancement in the thermally activated free carriers and ion mobilities.

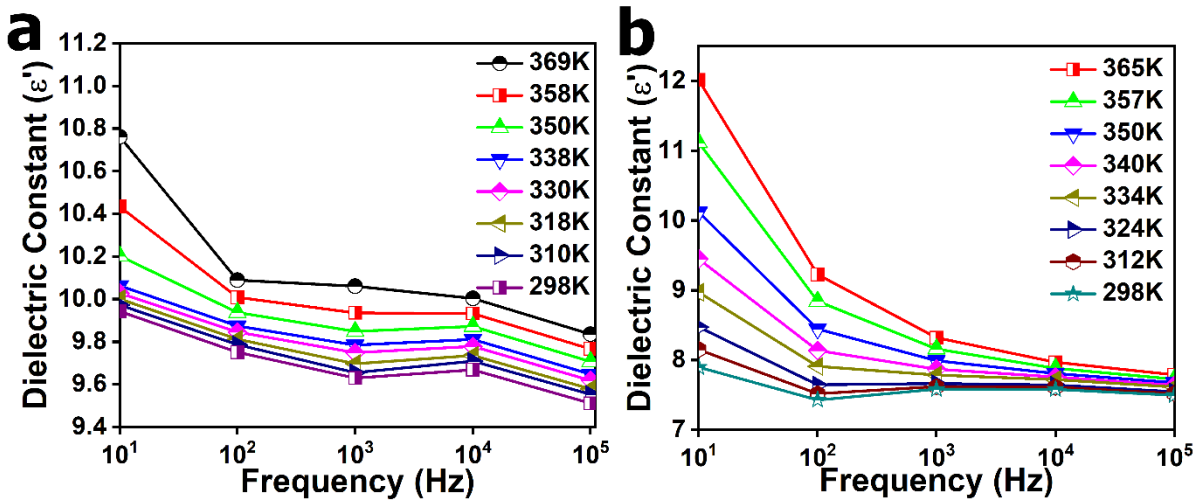

Figure 14: Frequency dependence of dielectric constant a)**1** and b) **2**.

Similar trends were observed in the frequency dependant dielectric profiles [Figure 14] of **1** and **2**. The ε' values showed a decreasing tendency while increasing the frequency from 10-10^5 Hz. Higher ε' values at lower frequencies indicate the involvement of all types of polarization mechanisms (Electronic, ionic, orientational and space charge polarizations). Higher relative permittivity values at low-frequency regions can be due to interfacial space charge formation.

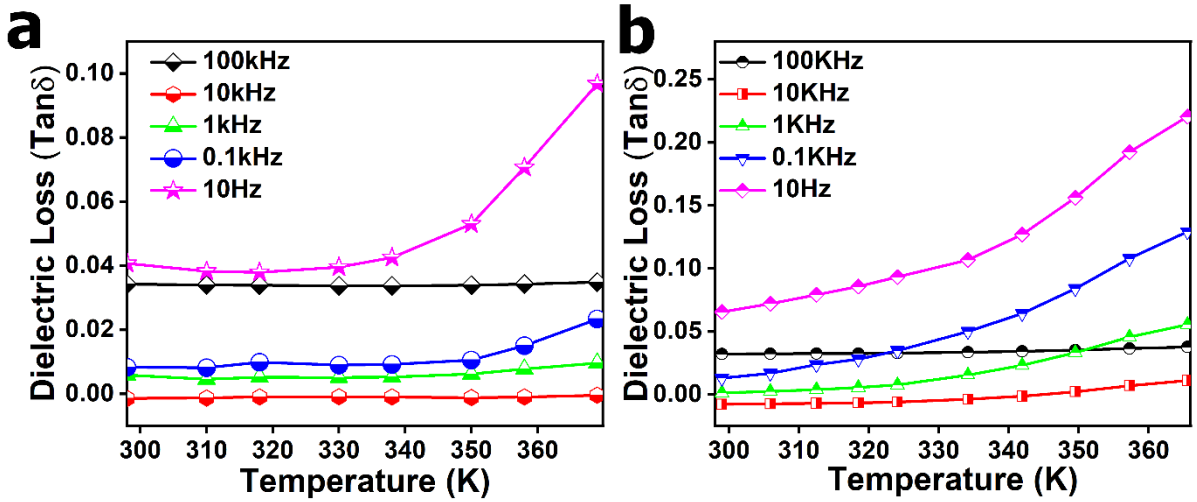

Figure 15: Temperature dependence of Tanδ a)**1** and b) **2**.

Similar trends were observed in the temperature and frequency dependant dielectric loss plots. Compounds **1** and **2** showed low dielectric loss behaviour for temperature and frequency dependant measurements [Figures 15 and 16]. The thermal motion of dipoles at higher temperatures can increase dielectric loss at high-temperature regions. Similarly, the higher dielectric loss behaviour of compound **1** and **2** at a lower frequency (10 Hz) can be due to the polarization contribution from all four polarization mechanisms.

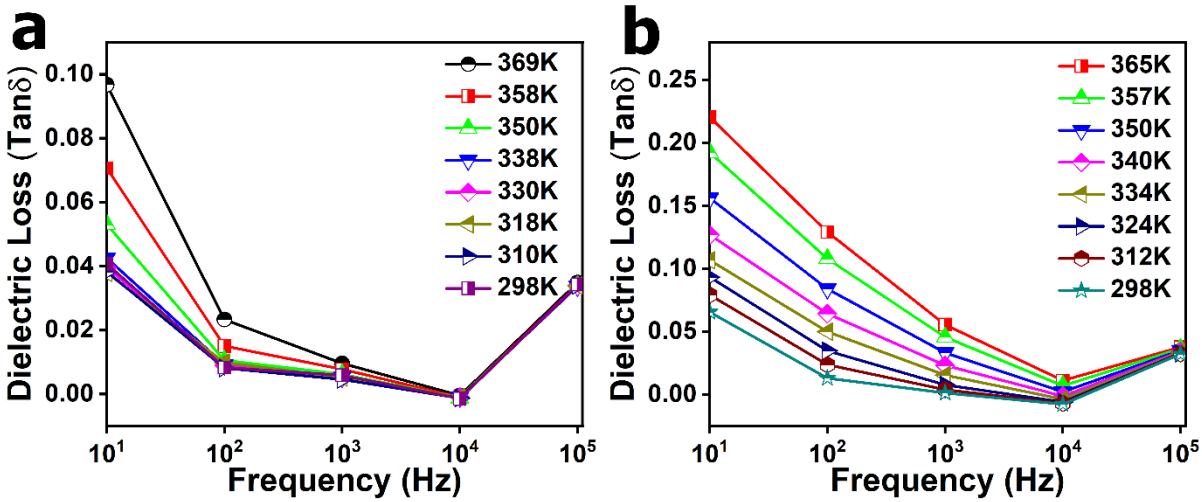

Figure 16: Frequency dependence of Tanδ a)**1** and b) **2**.

3.6 Hirshfeld Surface Properties of 1 and 2:

The intermolecular and intramolecular H-bonding interactions present in **1** and **2** were quantified by Hirshfeld surface analysis using the Crystal explorer 3.1 program. Here d_i denotes the corresponding distance of Hirshfeld surface to the nearest inside the nucleus, and d_e indicates the length of Hirshfeld surface to the nearest outside nucleus. So, d_e gives information about the packing of crystal around the surface and the nature of intermolecular contacts in the molecule. d_{norm} is the sum of the normalised contact of d_i and d_e. The curvedness here is a function of the curvature of the surface. Low curvedness denotes flat areas of the surface, and high curvedness denotes sharp curvature areas.

Areas with low curvedness have a lower tendency to divide the surface into contact patches with their neighbouring molecule compared to regions with high curvedness. The coordination number of a crystal can be defined using this. Shape index is the shape measure of crystal, which is very sensitive to a slight change in surface shape at low curvedness surface. It can be used to recognize hollows and bumps in the molecule [Figure 17-Figure 18].

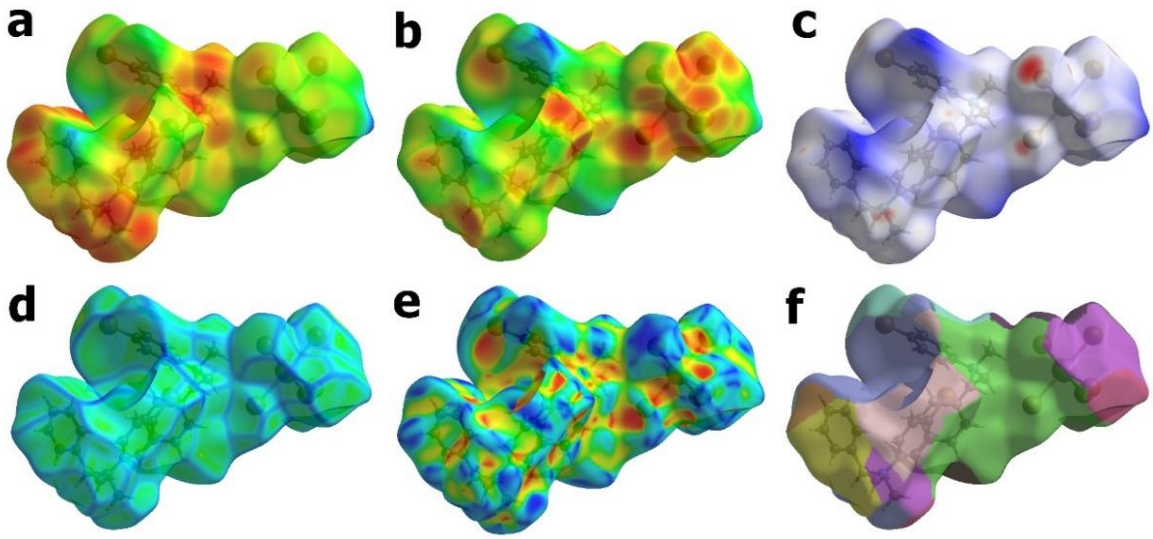

Figure 17: The (a) d_i, (b) d_e, (c) d_{norm}, (d) Curvedness, (e) Shape Index, and (f) Fragment Patch Hirshfeld Surfaces for compound **1**.

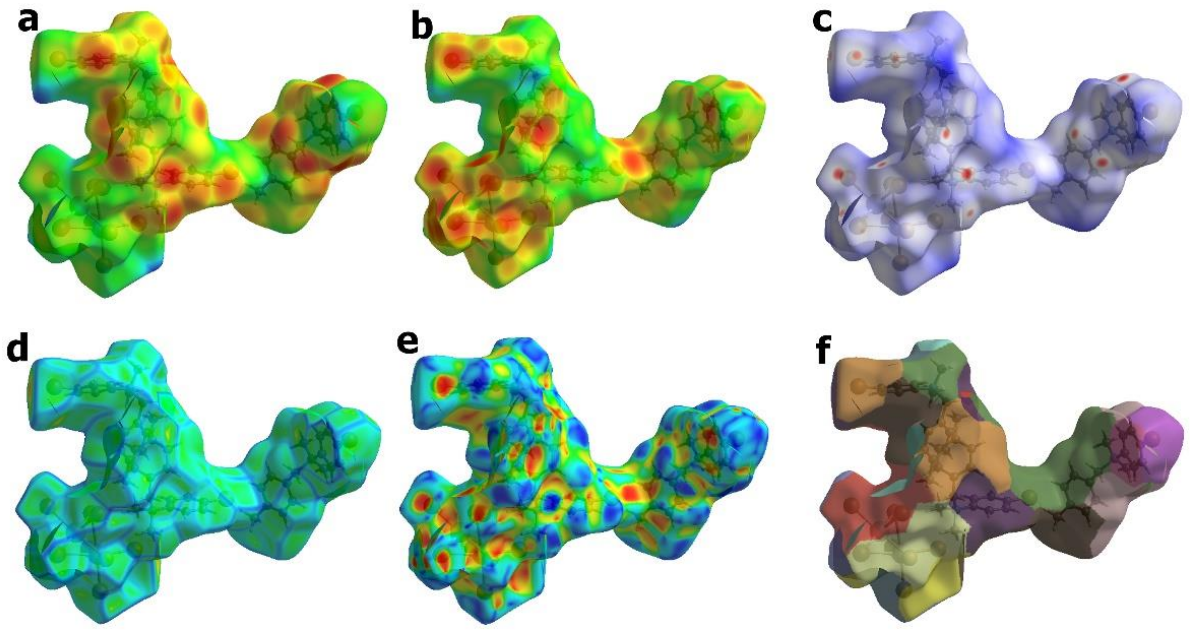

Figure 18: The (a) d_i, (b) d_e, (c) d_{norm}, (d) Curvedness, (e) Shape Index, and (f) Fragment Patch Hirshfeld Surfaces for compound **2**.

Intramolecular Interactions present in 1:

The dark red coloured parts on the d_{norm} surfaces refer to the strongly contributing interactions in the molecule while blue colour is for weak interactions present in the molecule. The uncoloured parts have zero contribution in such interactions.

Additionally, the associated 2D fingerprint plots were also mapped for compound **1**, showing the percentages of interactions (H···Br, H···H, and Br···Br) present in the molecule [Figure 19]. It tells us about intermolecular interactions present in the crystal and the relative surface area of these interactions. The 2D-fingerprint plot corresponds to a unique (d_e, d_i) pair.

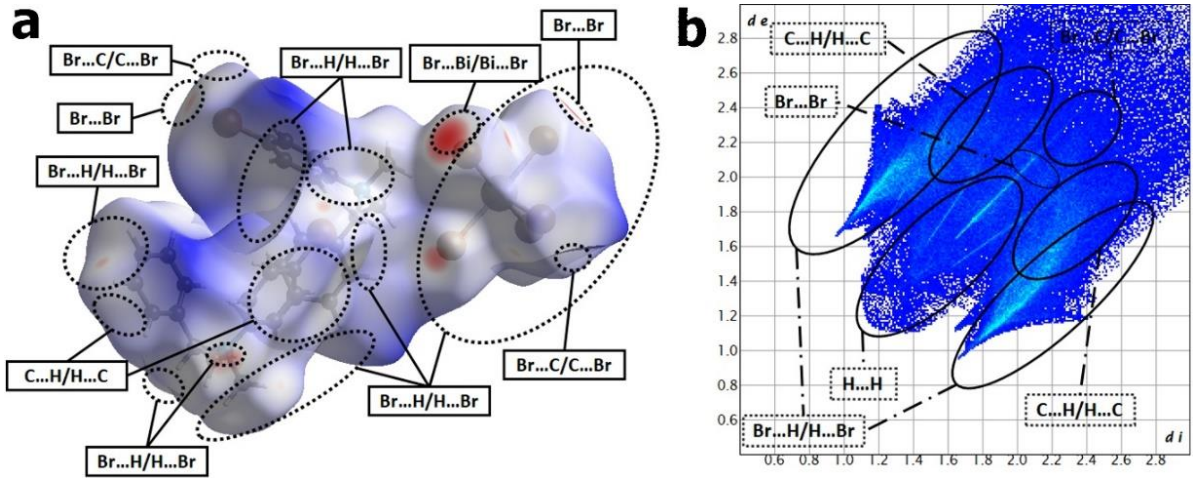

Figure 19: (a) Hirshfeld d_{norm} surfaces and (b) 2D fingerprint plot showing all interactions present in **1**.

The structure corresponds to C-H···Br contacts are most prominent type of contacts; From the overall of 53% contacts were contributed to hirshfeld surface by them. The contribution of H···H interaction to the entire hirshfeld surface (HS) is 30.3% which lies in the middle of 2D fingerprint plots. While C···H/H···C contacts contributing 10.3 % to the hirshfeld surface [Table 2].

For a better understanding of the interactions present in **1**, only the cations with comparatively stronger contacts in the structures were taken into account [Figure 20].

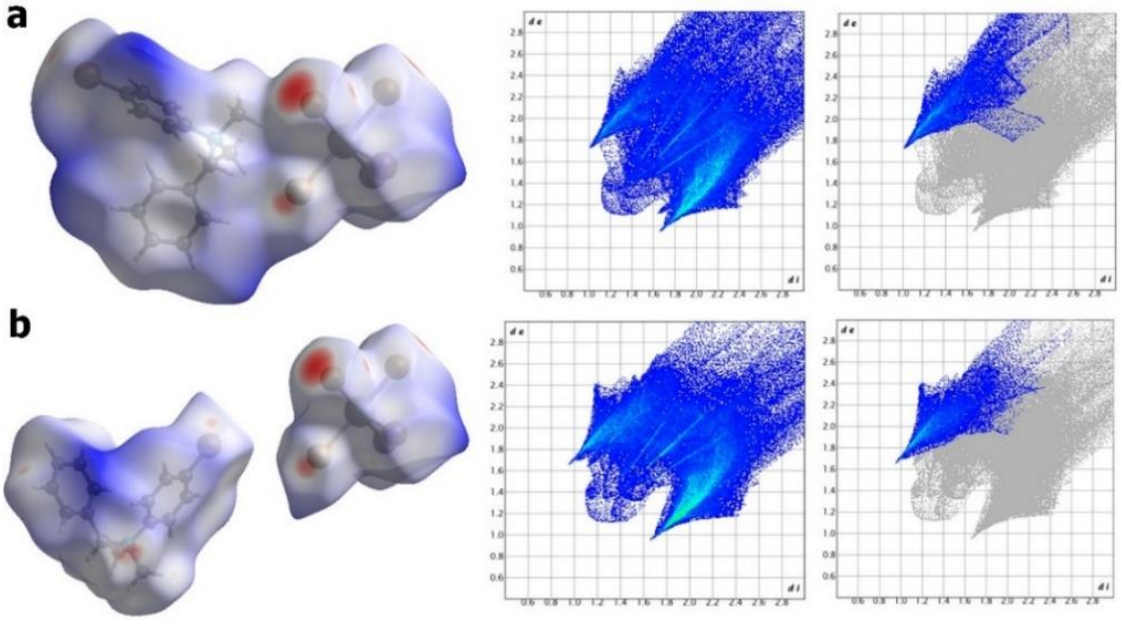

Figure 20**:**Hirshfeld d_{norm} surfaces (Left), 2D fingerprint plots for all interactions (middle) and 2D fingerprint plots for H_{inside}−$Br_{outside}$ interactions (right). (a) cation 1**,** (b) cation 2.

From the hirshfeld analysis of cation 1 and cation 2, the H_{inside}-$Br_{outside}$ interactions were again reflected in the 2D fingerprint plots, which gave shorter (minimum) d_i and d_e of 1.02, 1.72.and 0.93, 1.64, respectively [Figure 20right].

These analyses confirm that the contacts of cation 2 are obviously stronger than cation 1 and the fact that cation 2 contributes the maximum percentage of H···Br interactions present in the molecule.

Intramolecular Interactions present in 2**:**

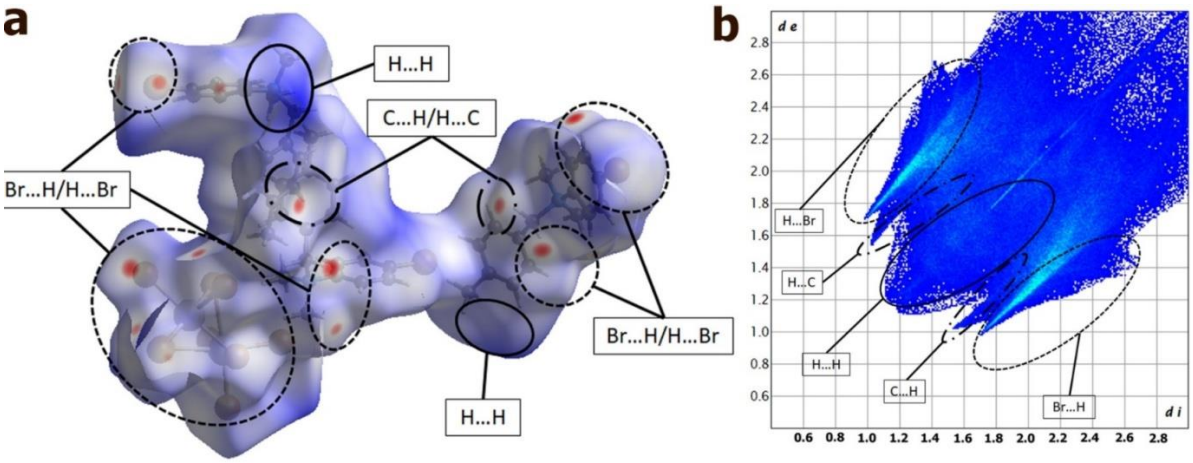

Figure 21**:** (a) Hirshfeld d_{norm} surfaces and (b) 2D fingerprint plot for all interactions present in **2**.

Similarly, the hirshfeld d_{norm} surfaces and 2D fingerprint plots of the associated cations in molecule **2** were further mapped and compared [Figure 21].

The most prominent type of contact in **2** is C-H···Br; they contribute 53.7 % of the overall surface contacts. The C···H/H···C contacts in the fingerprint plot contributing 9.8 % to the HS.

While the contribution of H···H interaction to the entire HS is 39.9 % which lies in the middle of 2D fingerprint plot (all interactions) [Table 4].

Again, to get better clarity about the interactions present in **2**, we focused on the cations with comparatively stronger contacts in the molecule.

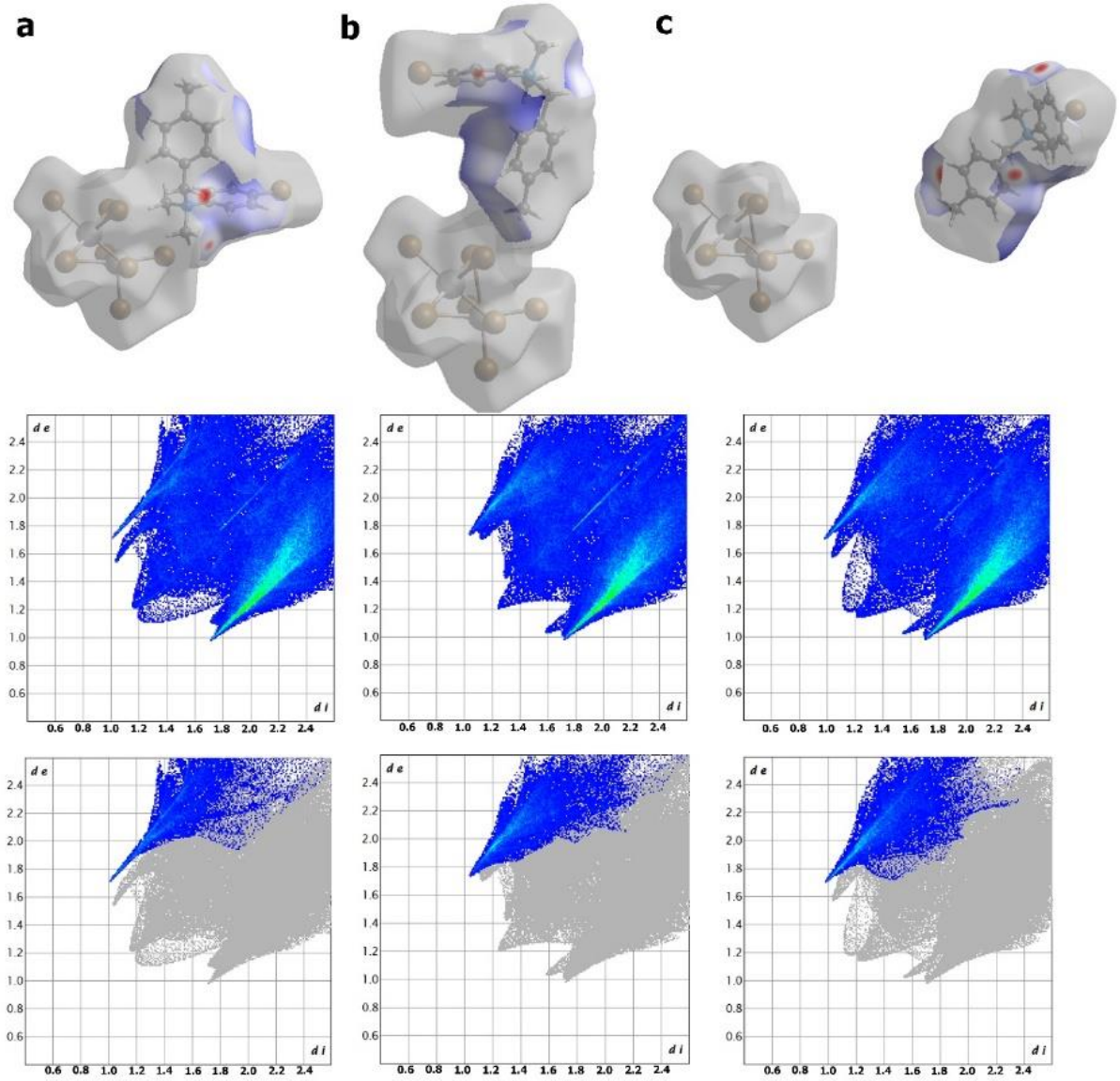

Figure 22: d_{norm} surfaces (Top), 2D fingerprint plots for all interactions (middle) and 2D fingerprint plots for H_{inside}–$Br_{outside}$ interactions (Bottom). (a) cation 1, (b) cation 2 and (c) cation 3.

The H_{inside}-$Br_{outside}$ interactions were also reflected by the 2D fingerprint plots, which have shorter minimum d_i and d_e of 1.0 and 1.72 in cation 1, 1.02 and 1.73 in cation 2 and 0.97 and 1.72 in cation 3, respectively [Figure 22bottom].

The cation 3 has the strongest H-bonding interactions with the Br atoms of Bi_2Br_9 moiety than cation 1 and cation 2.

3.7 Fabrication and Characterisations of 1-PLA and 2-PLA Composite Films:

To examine the energy-harvesting properties of **1** and **2**, their polymer composite films were prepared with polylactic acid (PLA). For this purpose, appropriate quantities (5, 10, 15, and 20 wt%) of compounds **1** and **2** were dispersed in a chloroform solution of PLA. Then homogeneous solutions were poured onto the petri-dish and dried. The dried composite films were peeled off and used for applications like mechanical energy harvesting. The intact nature of ferroelectric crystallites in these polymer matrixes were then examined by PXRD analyses. The PXRD profiles of **1-PLA** and **2-PLA** composites confirmed the crystalline nature of **1** and **2** in the PLA matrix with increasing intensity of peaks upon increasing the crystallite loadings (5 to 20 wt%) onto the polymer matrix [Figure 23]. All polymer composite films of **1-PLA** and **2-PLA** exhibit excellent flexibility.

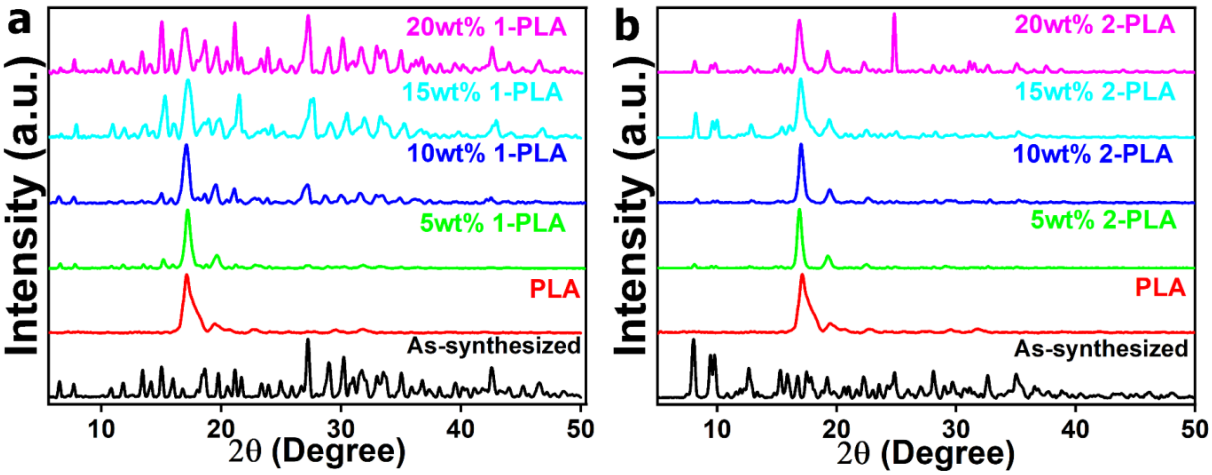

Figure 23: Stacked PXRD profile (synthesized and composite films) for different wt% a) **1** and b) **2** in PLA.

The FE-SEM technique was used to further visualise the composite films' structural morphologies, which showed an even dispersal of the ferroelectric particles up to 15 wt% and 10 wt% in the composite films, respectively for **1-PLA** and **2-PLA**.

However, agglomeration of the particles was confirmed by FE-SEM images in the case of composite with 20 wt% of **1-PLA** and 15 wt%, 20 wt% for **2-PLA** [Figure 24].

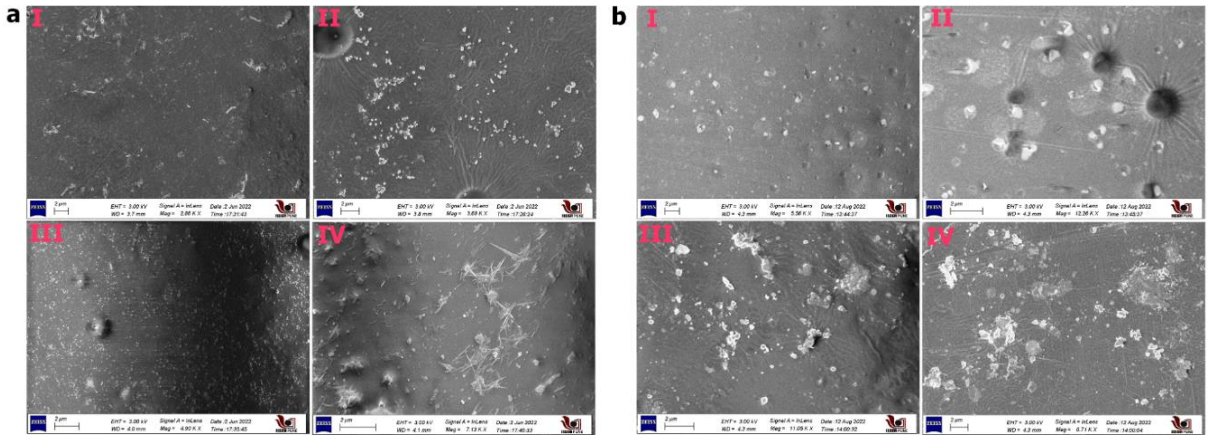

Figure 24: FE-SEM profile for different wt% (a) **1** and (b) **2** in PLA {i- 5 wt%, ii- 10 wt%, iii- 15 wt%, iv- 20 wt%}

3.8 Construction of piezoelectric device for energy harvesting:

All weight percentage films were cut into an identical rectangular shape of dimension 3 cm×1 cm for **1-PLA** and **2-PLA** films. Adhesive copper tapes were used as bottom and top electrodes and the copper wires were soldered on the edge of these tapes. An outer layer of Kapton tape has been used to protect these devices from static surface charges generated during piezoelectric measurement. All the measurements were carried out using a custom-built impact force setup connected with an oscilloscope for voltage measurement.

3.9 Piezoelectric Studies:

Outputs of 1-PLA Composite Devices from Mechanical Energy Harvesting:

The mechanical energy harvesting measurements **1-PLA** were done with an optimized applied external load of 21 N and at 10 Hz constant frequency. The open-circuit peak-to-peak voltages (V_{PP}) were observed to be 8.5, 11.06, 26.2, and 17.13 V for the composite devices of 5, 10, 15 and 20 wt% **1-PLA** [Figure 25].

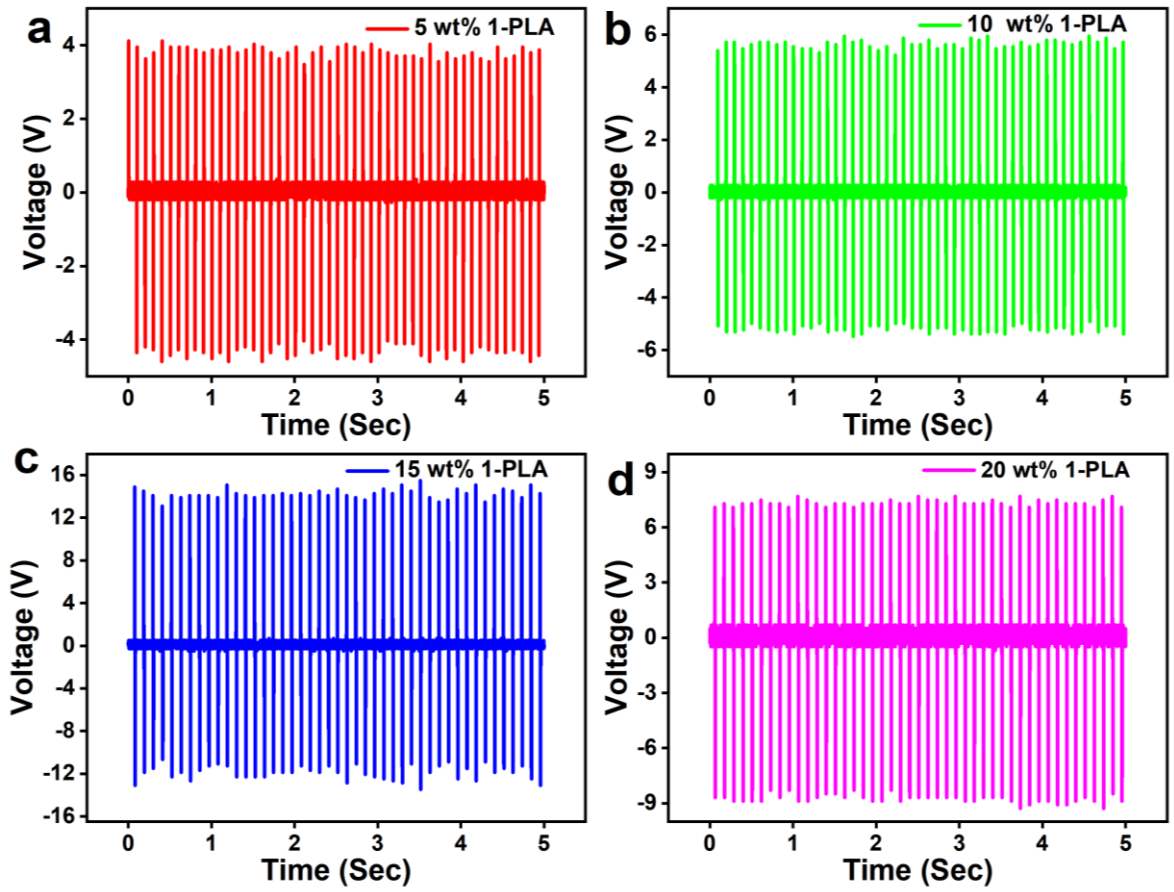

Figure 25: V_{PP} profile of different weight percentage devices.

The maximum V_{PP} was observed to be 26.2 V for the 15 wt% **1-PLA** device. In contrast, the device with neat PLA gave a minimal voltage of 2.04 V owing to its piezoelectric nature.
This confirms that the increase in voltage output is due to the addition of ferroelectric crystallites of **1** into PLA polymer matrix.

Again, to validate the practical utility of these devices, the voltage drops were measured using different external load resistors ranging from 0.11 to 88 MΩ. An increasing trend in output voltage has been seen while increasing resistance until 22 MΩ, and after that, it starts to saturate.

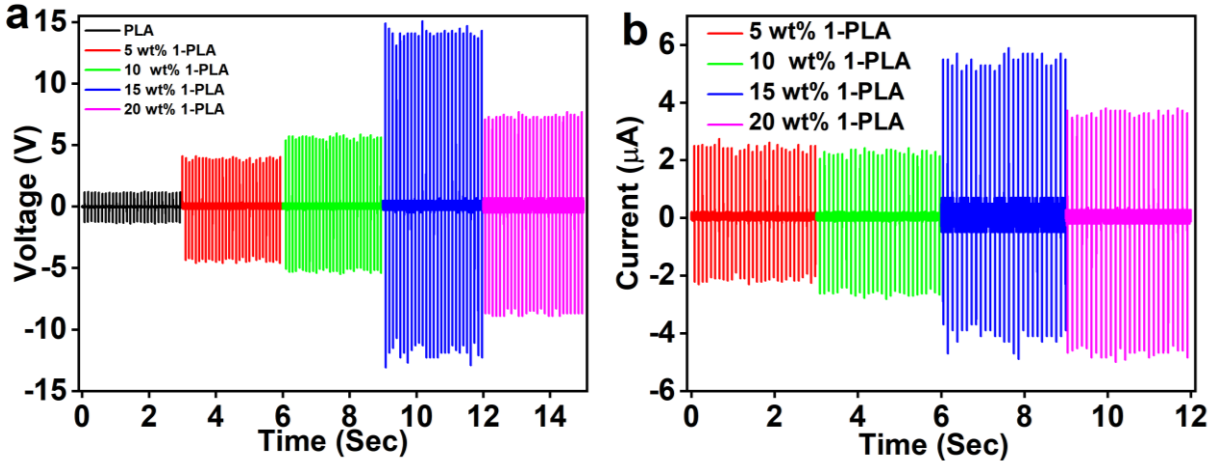

Figure 26: (a) V_{PP} and (b) I_{PP} profiles for different weight percentage devices.

Short circuit peak-to-peak current (I_{PP}) were calculated using the equation ($v = IR$), at an external 1 MΩ resistance. The calculated currents were found to be 4.59, 5.03, 10.63, and 8.29 μA respectively for the 5, 10, 15 and 20 wt% **1-PLA** devices [Figure 26].

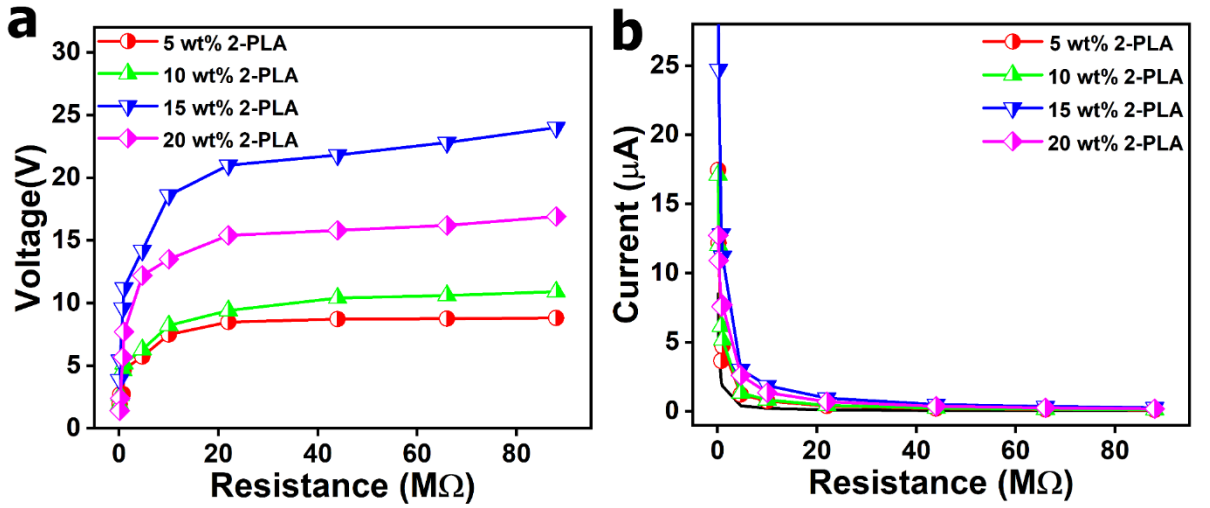

Figure 27: (a) voltage and (b) current profiles with resistance for different weight percentage devices.

The increasing trend in V_{PP} and I_{PP} with increasing percentage loading up to 15 wt% was observed, while a decrease in output was seen for the 20 wt% of **1-PLA** device.
This reduction in output performance can be attributed to the agglomeration of the ferroelectric particles in the PLA matrix at higher weight percentages.

The power density and current density were also calculated for various load resistances across the devices. The maximum power density and current density were calculated to be 41.81 $\mu W.cm^{-2}$ and 3.73 $\mu A.cm^{-2}$, respectively, for 15 wt% **1-PLA** device with 1 MΩ resistor [Figure 28].

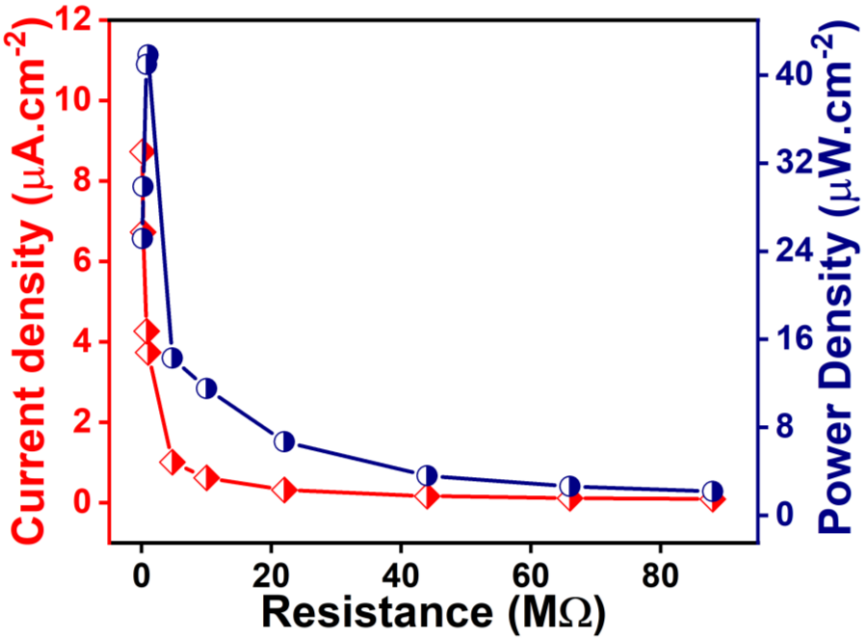

Figure 28: Power density and Current density of the 15 wt% **1–PLA** composite devices.

The cyclic stability measurements were also done to visualize the robustness of the optimum 15 wt% **1-PLA** device. Retention in voltage output was seen for up to 3000 cycles with a constant external impact of 21 N [Figure 29].

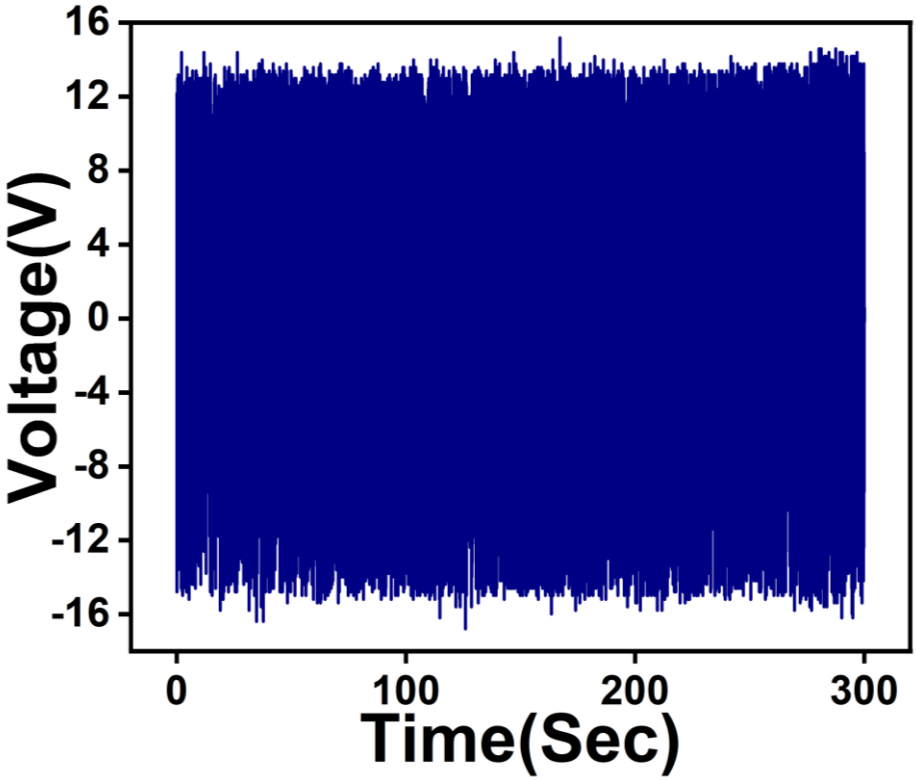

Figure 29: Durability of the device up to 3000 cycles.

The 15 wt% **1-PLA** device was then utilized to charge two different capacitors (10 and 100 µF) to check its practical use. For this purpose, the AC output signals were converted into DC voltage using a bridge rectifier circuit made up of four diodes.

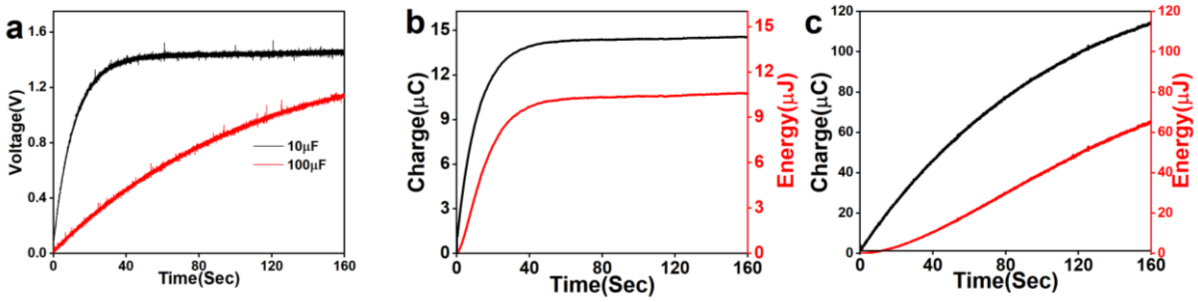

Figure 30**:** (a) Voltage profile, Charge and energy profile for (b) 10µF and (c) 100µF.

The maximum stored voltages were 1.45 V and 1.15 V (160 seconds) for 100 µF and 10 µF, respectively, while applying the continuous external force of 21 N. The measured maximum charge ($Q = CV$) and energy ($E = \frac{1}{2}CV^2$) stored in the capacitors were calculated to be 114 µC and 64 µJ, respectively, for 100 µF. For the 10 µF capacitor, the charge and maximum energy were calculated to be 14 µC and 10 µJ, respectively [Figure 30].

Outputs of 2-PLA Composite Devices from Mechanical Energy Harvesting:

Similarly, with the same external load of 21 N and at a constant 10 Hz frequency, the energy harvesting outputs were collected for all the **2-PLA** composite devices in the non-poled state.

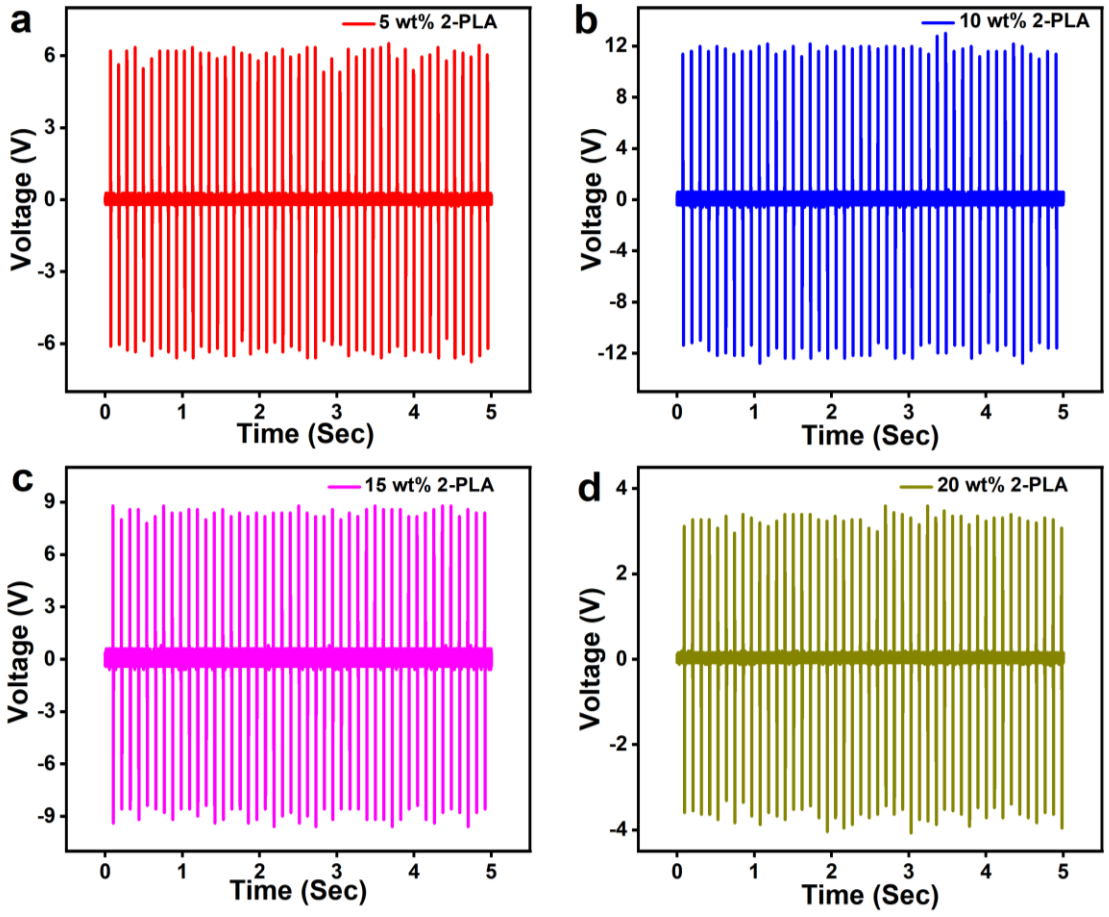

Figure 31: V_{PP} profile of different weight percentage devices.

The maximum V_{PP} were measured to be 13.76, 24.06, 18.34, and 7.17 V for the 5, 10, 15, and 20 wt% **2-PLA,** respectively [Figure 32].

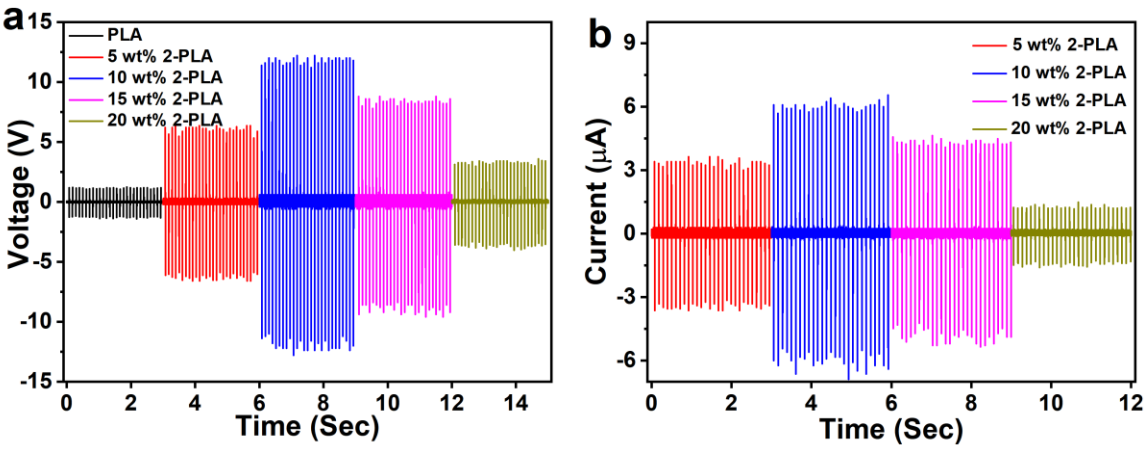

Figure 32: (a) V_{PP} and (b) I_{PP} profiles for different weight percentage devices.

Again, V_{PP} for all the devices were measured using different external load resistors ranging from 0.11 to 88 MΩ. An increasing trend in output voltage has been seen while increasing resistance until 11 MΩ, and after that, saturation was observed. Short-circuit current (I_{PP}) were calculated at an external resistance of 1 MΩ for the resistance [Figure 32]. The calculated peak-to-peak short-circuit current (I_{PP}) were 6.76, 12.01, 9.49, and 2.67 μA for the 5, 10, 15, and 20 wt% of **2-PLA** composite devices.

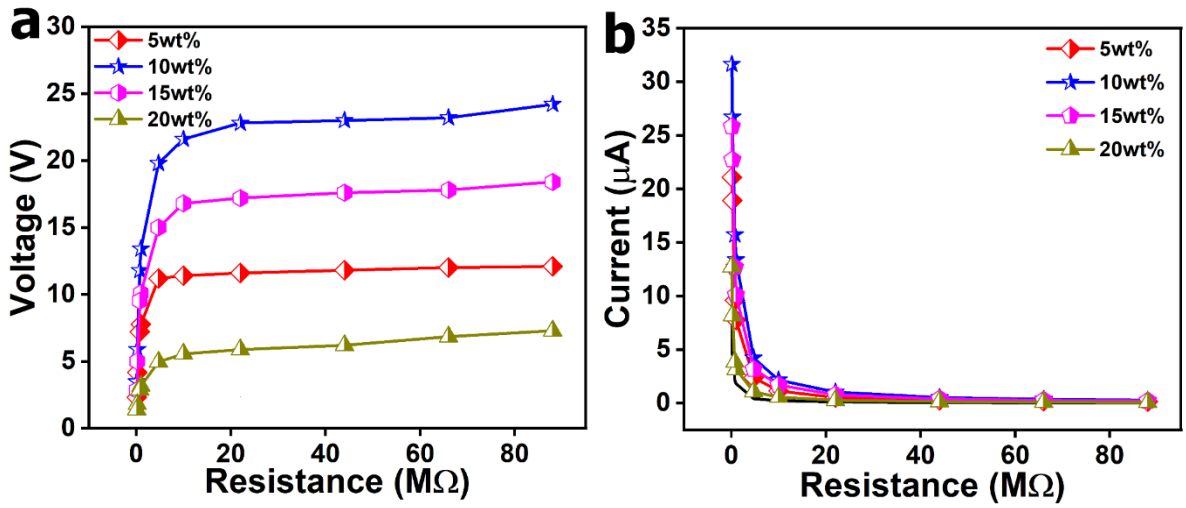

Figure 33**:** (a) voltage and (b) current profiles with resistance for different weight percentage devices.

The increasing trend in V_{PP} and I_{PP} was observed up to 10 wt% and afterward, for 15 and 20 wt% of **2-PLA** devices decrease in output was seen.

This can be attributed to the agglomeration of ferroelectric crystallites at 15 and 20 wt% loading in the polymer matrix. The aggregation results in the cancellation of dipoles and hence decrease in output performance.

The calculated power density and current density profiles followed a similar trend of voltage with different weight percentages.

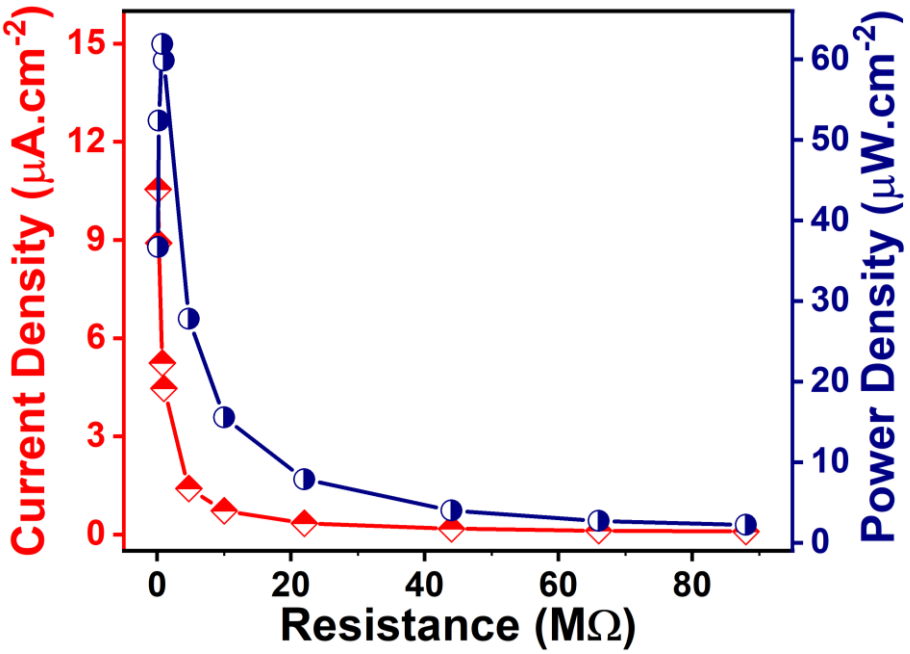

Figure 34: : Power density and Current density of the 10 wt% **2–PLA** composite devices.

The maximum power density and current density were calculated to be 61.88 $\mu W.cm^{-2}$ and 5.24 $\mu A.cm^{-2}$, respectively, for the optimum 10 wt% **2-PLA** device with 750 kΩ resistor [Figure 34].

To check the device's depletion of voltage and durability, a fatigue test was performed, where retention in voltage was seen up to 5000 cycles [Figure 35].

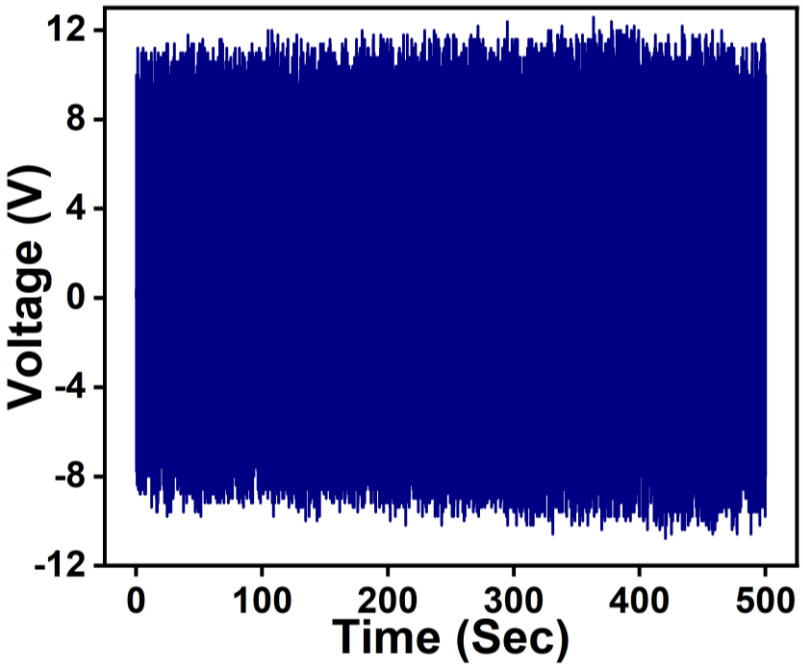

Figure 35: Durability of 10 wt% device up to 5000 cycles.

The practical utility of the 10 wt% **2-PLA** was examined by charging two capacitors of the order of 10 and 100 µF using a four-diode bridge rectifier circuit.

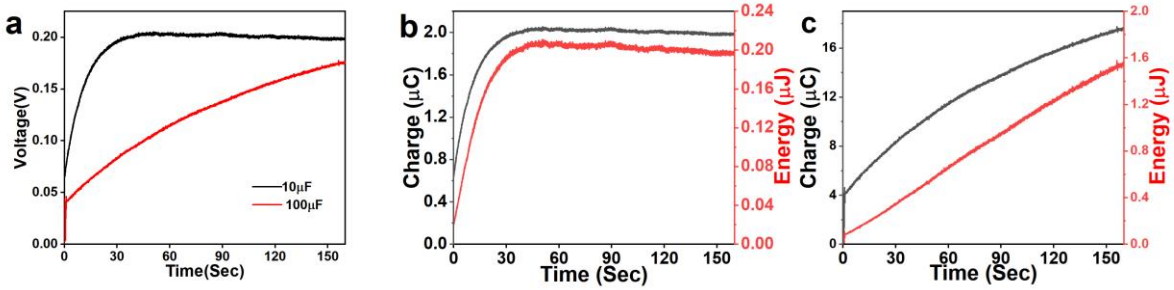

Figure 36**:** (a) Voltage profile, Charge and energy profile for (b) 10µF and (c) 100µF.

The maximum stored voltages were 0.2 V and 0.15 V (160 seconds) for 100 µF and 10 µF, respectively. The calculated maximum stored energy (E) and charge (Q) in the capacitors are 1.78 µJ and 18.92 µC, respectively, for 100 µF. Similarly, for the 10 µF capacitor, 0.20 µJ of energy and 2.03 µC of maximum charge have been stored using the 10 wt% **2-PLA** device [Figure 36].

4 Conclusion

In summary, we have successfully designed two new hybrid ammonium perovskites $[[BrPhBnN(Me)_2]_2.[BiBr_5]$ and $[BrPhMeBnN(Me)_2]_3.[Bi_2Br_9]$. The ammonium halogenobismuthates **1** and **2** were found to crystallize in the polar point groups *Pna21* and *Pca21*, respectively. We further investigated the second harmonic generation (SHG), dielectric, and piezoelectric properties of these two compounds. For **1** and **2**, the dielectric constants were found to be 9.51 and 7.49 at room temperature and 100 kHZ frequency. Additionally, the polar nature of these two materials is confirmed from the obtained dipole moments 37.10 and 115.07 Debye, respectively for **1** and **2**. Moreover, their subsequent implementation for mechanical energy harvesting applications in the form of PLA polymer composites results in maximum peak-to-peak voltages of 26.2 and 24.06 V respectively form compound **1** and **2** for an applied frequency of 10 Hz and impact force of 21 N. Also the maximum power density values were calculated to be 41.81 and 61.88 $\mu W.cm^{-2}$ for the optimal 15 wt% **1-PLA** and 10 wt% **2-PLA** devices, respectively. The capacitor charging capabilities of the devices were also demonstrated. These findings lay out a promising platform for designing new lead-free ammonium-based perovskites for future self-powered electronics.

Table 1: Details of crystallographic data collection of 1

	Low Temperature	Room Temperature
Chemical formula	$C_{30}H_{34}BiBr_7N_2$	$C_{30}H_{34}BiBr_7N_2$
Formula weight	1190.94	1190.94
Temperature	273(2) K	303(2) K
Crystal system	Orthorhombic	Orthorhombic
Space group	*Pna21*	*Pna21*
Unit cell dimensions	a = 18.09Å, b = 23.78Å, c = 9.04Å. α=90°, β= 90°, γ = 90°.	a = 18.34Å, b = 24.13Å, c = 9.23Å. α=90°, β= 90°, γ = 90°.
Volume	3894(6) $Å^3$	4089(2) $Å^3$
Z	4	4
Density (calculated)	4.985 $Mg.m^{-3}$	1.934 $Mg.m^{-3}$
Absorption coefficient	51.155 mm^{-1}	11.171 mm^{-1}
F(000)	4884	2224
Theta range for data collection	18.727°.	22.419°.
Independent reflections	R_{int} = 0.4948	R_{int} = 0.0865
Completeness	0.966	0.998
Data / restraints / parameters	2861/ 610/223	5256/217/317
GOF on F2	1.056	1.17
Final R indices	R1 = 0.0994, wR2 = 0.2227	R1 = 0.0356, wR2 = 0.0993
Largest diff. peak and hole	2.382/ -1.448e.$Å^{-3}$	1.491/ -0.937e.$Å^{-3}$

Table 2:Percentage of all interactions present in compound 1.

Inside	**Outside**	**Atom**				
Atom	**BI**	**BR**	**N**	**C**	**H**	
BI	.	0.8	.	.	0.2	0.9
BR	0.7	2.3	.	1.1	30.3	34.4
C	.	1.0	.	0.5	5.5	7.1
H	0.0	22.3	.	4.8	30.3	57.5
N	.	.	.	.	.	0.0
	0.7	26.5	0.0	6.5	66.4	

Table 3: Details of crystallographic data collection of 2:

	Low Temperature	Room Temperature
Chemical formula	$C_{48}H_{57}Bi_2Br_{12}N_3$	$C_{48}H_{57}Bi_2Br_{12}N_3$
Formula weight	2052.84	2052.84
Temperature	273(2) K	303(2) K
Crystal system	Orthorhombic	Orthorhombic
Space group	*Pca21*	*Pca21*
Unit cell dimensions	a = 28.351(4)Å, b = 11.9182(14)Å, c = 18.503(2)Å	a = 28.882(7)Å, b = 12.096(3)Å, c = 18.538(4)Å
	α= 90°, β= 90°, γ= 90°,	α= 90°, β= 90°, γ= 90°,
Volume Å^3	6252.1(13)	6477(3)
Z	4	4
Density (calculated) Mg.m^{-3}	2.181	2.105
Absorption coefficient mm^{-1}	13.323	12.861
F(000)	3808	3808
Theta range for data collection	1.436 to 18.879°.	1.410 to 28.413°.
Independent reflections	R_{int} = 0.1416	R_{int} = 0.3693
Completeness to theta	99.70%	100.00%
Data / restraints / parameters	4919/1034/409	16193 / 1 / 505
GOF on F2	1.082	0.974
Final R indices [I>2sigma(I)]	R1 = 0.0533, wR2 = 0.1251	R1 = 0.0810, wR2 = 0.1829
Largest diff. peak and hole e.Å^{-3}	3.331 and -1.172	2.014 and -1.993

Table 4: Percentage of all interactions present in compound 2.

Inside	**Outside Atom**					
Atom	**BI**	**BR**	**N**	**C**	**H**	
BI	.	.	.	.	.	0.0
BR	.	1.7	.	2.1	31.5	35.4
C	.	2.0	.	0.7	5.3	8
H	.	22.2	.	4.5	39.9	56.6
N	.	.	.	.	.	0.0
	0.0	26.0	0.0	7.3	66.7	

References

1. Rosenberg, H. J. M. S.; Engineering, r. e., The Solid State: An Introduction to the Physics of Crystals for Students of Physics. **1988**, 326.
2. Dorey, R. J. C. T. F. f. M.; Microdevices, M.; Technologies, N., Microstructure–property relationships: How the microstructure of the film affects its properties. **2012**, 85-112.
3. Shi, P.-P.; Tang, Y.-Y.; Li, P.-F.; Liao, W.-Q.; Wang, Z.-X.; Ye, Q.; Xiong, R.-G. J. C. S. R., Symmetry breaking in molecular ferroelectrics. **2016,** *45* (14), 3811-3827.
4. Valasek, J., Piezo-Electric and Allied Phenomena in Rochelle Salt. *Physical Review* **1921,** *17* (4), 475-481.
5. Busch, G.; Scherrer, P. J. N., Eine neue seignette-elektrische Substanz. **1935,** *23* (43), 737-737.
6. Von Hippel, A.; Breckenridge, R.; Chesley, F.; Tisza, L. J. I.; Chemistry, E., High dielectric constant ceramics. **1946,** *38* (11), 1097-1109.
7. Shirane, G.; Suzuki, K.; Takeda, A. J. J. o. t. P. S. o. J., Phase transitions in solid solutions of PbZrO3 and PbTiO3 (II) X-ray study. **1952,** *7* (1), 12-18.
8. Shirane, G.; Takeda, A. J. J. o. t. P. S. o. J., Phase transitions in solid solutions of PbZrO3 and PbTiO3 (I) small concentrations of PbTiO3. **1952,** *7* (1), 5-11.
9. Zhang, Y.; Xie, M.; Roscow, J.; Bao, Y.; Zhou, K.; Zhang, D.; Bowen, C. R. J. J. o. M. C. A., Enhanced pyroelectric and piezoelectric properties of PZT with aligned porosity for energy harvesting applications. **2017,** *5* (14), 6569-6580.
10. Wang, B.; Ma, D.; Zhao, H.; Long, L.; Zheng, L. J. I. C., Room Temperature Lead-Free Multiaxial Inorganic–Organic Hybrid Ferroelectric. **2019,** *58* (20), 13953-13959.
11. Bowen, C., Enhanced pyroelectric and piezoelectric properties of PZT with aligned porosity for energy harvesting applications. **2019**.
12. Faustini, M.; Nicole, L.; Ruiz-Hitzky, E.; Sanchez, C. J. A. F. M., History of organic–inorganic hybrid materials: prehistory, art, science, and advanced applications. **2018,** *28* (27), 1704158.
13. Chin, X. Y.; Cortecchia, D.; Yin, J.; Bruno, A.; Soci, C., Lead iodide perovskite light-emitting field-effect transistor. *Nature Communications* **2015,** *6* (1), 7383.
14. Yoo, E. J.; Lyu, M.; Yun, J.-H.; Kang, C. J.; Choi, Y. J.; Wang, L., Resistive Switching Behavior in Organic–Inorganic Hybrid CH3NH3PbI3−xClx Perovskite for Resistive Random Access Memory Devices. **2015,** *27* (40), 6170-6175.
15. Sebastian, M. T., *Dielectric materials for wireless communication*. Elsevier: 2010.
16. Maeder, M. D.; Damjanovic, D.; Setter, N. J. J. o. E., Lead free piezoelectric materials. **2004,** *13* (1), 385-392.
17. Vijayakanth, T.; Srivastava, A. K.; Ram, F.; Kulkarni, P.; Shanmuganathan, K.; Praveenkumar, B.; Boomishankar, R. J. A. C., A Flexible Composite Mechanical Energy Harvester from a Ferroelectric Organoamino Phosphonium Salt. **2018,** *130* (29), 9192-9196.
18. Vijayakanth, T.; Pandey, R.; Kulkarni, P.; Praveenkumar, B.; Kabra, D.; Boomishankar, R. J. D. T., Hydrogen-bonded organo-amino phosphonium halides: dielectric, piezoelectric and possible ferroelectric properties. **2019,** *48* (21), 7331-7336.
19. Vijayakanth, T.; Ram, F.; Praveenkumar, B.; Shanmuganathan, K.; Boomishankar, R. J. C. o. M., All-Organic Composites of Ferro-and Piezoelectric Phosphonium Salts for Mechanical Energy Harvesting Application. **2019,** *31* (15), 5964-5972.
20. Vijayakanth, T.; Ram, F.; Praveenkumar, B.; Shanmuganathan, K.; Boomishankar, R. J. A. C. I. E., Piezoelectric Energy Harvesting from a Ferroelectric Hybrid Salt [Ph3MeP] 4 [Ni (NCS) 6] Embedded in a Polymer Matrix. **2020,** *59* (26), 10368-10373.
21. Sahoo, S.; Deka, N.; Boomishankar, R. J. C., Piezoelectric energy harvesting of a bismuth halide perovskite stabilised by chiral ammonium cations. **2022,** *24* (35), 6172-6177.

22. Deswal, S.; Singh, S. K.; Rambabu, P.; Kulkarni, P.; Vaitheeswaran, G.; Praveenkumar, B.; Ogale, S.; Boomishankar, R. J. C. o. M., Flexible composite energy harvesters from ferroelectric A2MX4-type hybrid halogenometallates. **2019,** *31* (12), 4545-4552.
23. Sheldrick, G. M. J. A. C. S. A. F. o. C., A short history of SHELX. **2008,** *64* (1), 112-122.
24. Wen Zhang and Ren-Gen Xiong, *Chem. Rev.* **2012**, *112* (2), 1163–1195
25. https://blog.knowlescapacitors.com/blog/capacitor-fundamentals-part-4-dielectric-polarization
26. https://personales.unican.es/junqueraj/JavierJunquera_files/Talks/COH-09.pdf